Extended hopanoid loss reduces bacterial motility and surface attachment and leads to heterogeneity in root nodule growth kinetics in a *Bradyrhizobium-Aeschynomene* symbiosis

Belin, B.J.,[1] Tookmanian, E.T.,[2] de Anda, J.,[4] Wong, G. C. L.,[4] Newman, D.K.[1,3]

[1]Division of Biology & Bioengineering, [2]Division of Chemistry & Chemical Engineering, [3]Division of Geological & Planetary Sciences, California Institute of Technology, Pasadena, CA.

[4]Department of Bioengineering, Department of Chemistry and Biochemistry, and California NanoSystems Institute, University of California Los Angeles, Los Angeles, CA 90095-1600, USA University of California Los Angeles, Los Angeles, CA.

Abstract

Hopanoids are steroid-like bacterial lipids that enhance membrane rigidity and promote bacterial growth under diverse stresses. Hopanoid biosynthesis genes are conserved in nitrogen-fixing plant symbionts, and we previously found that the extended (C_{35}) class of hopanoids in *Bradyrhizobium diazoefficiens* are required for efficient symbiotic nitrogen fixation in the tropical legume host *Aeschynomene afraspera*. Here we demonstrate that the nitrogen fixation defect conferred by extended loss can fully be explained by a reduction in root nodule sizes rather than per-bacteroid nitrogen fixation levels. Using a single-nodule tracking approach to track *A. afraspera* nodule development, we provide a quantitative model of root nodule development in this host, uncovering both the baseline growth parameters for wild-type nodules and a surprising heterogeneity of extended hopanoid mutant developmental phenotypes. These phenotypes include a delay in root nodule initiation and presence of a subpopulation of nodules with slow growth rates and low final volumes, which are correlated with reduced motility and surface attachment *in vitro* and lower bacteroid densities *in planta*, respectively. This work provides a quantitative reference point for understanding the phenotypic diversity of ineffective symbionts in *A. afraspera* and identifies specific developmental stages affected by extended hopanoid loss for future mechanistic work.

28 **Introduction**

29 Hopanoids are steroid-like lipids that support bacterial survival under stress (reviewed in Belin et
30 al. 2018). They are synthesized by the squalene-hopene cyclase (*shc*) family of enzymes (Ochs et al.
31 1992; Syren et al. 2016), which generate the pentacyclic, C_{30} hopanoid core from squalene. In many
32 organisms, the C_{30} hopanoids can be further modified, including methylation at the C-2 position via the
33 enzyme HpnP (Welander et al. 2010) and addition of a ribose-derived side chain by the enzyme HpnH
34 (Fig. 1a) (Welander et al. 2012). Side chain-containing hopanoids are known collectively as the C_{35} or
35 "extended" hopanoids and commonly include molecules with aminotriol-, polyol-, and adenosyl- side-
36 chain moieties (Schmerk et al. 2015). Organism-specific side chains have also been observed, including
37 a hopanoid-lipid A conjugate known as HoLA (Silipo et al. 2014; Kulkarni et al. 2015; Komaniecka et al.
38 2014) that so far has only been found in *Bradyrhizobiaceae*.

39 It is thought that hopanoids primarily promote bacterial survival by rigidifying and decreasing the
40 permeability of membranes (Saenz et al. 2015;'Wu et al. 2015), providing a better barrier against external
41 stress. Structurally distinct hopanoids have different capacities to alter the biophysical properties of
42 membranes and can also differ in the degrees of stress resistance they confer (reviewed in Belin et al.
43 2018). In the *Bradyrhizobia* genus of legume symbionts, hopanoids promote growth of free-living cultures
44 under acid, salt, detergent, antibiotic, and redox stresses (Silipo et al. 2014; Kulkarni et al. 2015), and we
45 previously showed that these stress resistance phenotypes are largely mediated by the extended
46 hopanoid class (Kulkarni et al. 2015).

47 We also analyzed an extended hopanoid-deficient mutant of *Bradyrhizobium diazoefficiens*
48 USDA110 in symbiosis with two legumes: the native soybean host for this strain and *Aeschynomene*
49 *afraspera,* the native host of the closely related photosynthetic *Bradyrhizobia*. *A. afraspera* is a flood-
50 tolerant legume from tropical West Africa, where it has been used in rice intercropping systems (Somado
51 et al. 2003) and to accelerate wound healing in traditional medicine (Swapna et al. 2011; Chifundera
52 2001; Caamal-Fuentes et al. 2015; Lei et al. 2018). We found that extended hopanoid-deficient mutants
53 of *B. diazoefficiens* fixed less nitrogen per nodule in *A. afraspera* than wild type, while this strain did not
54 appear to have a defect in its native soybean host. Microscopy analyses of a small sample of extended
55 hopanoid mutant-infected *A. afraspera* nodules revealed several aberrant cytological phenotypes,

including both nodules containing necrotic signatures, disorganized infection zones, and visible starch granule accumulation (Kulkarni et al. 2015).

These phenotypes are common signatures of poor symbiont performance, yet the lack of genetic tools for *A. afraspera*, the limited literature on this host's response to non-cooperators compared to model plants, and low number of nodules examined made it difficult to determine the underlying cause. While it has been proposed that hopanoids may enable high rates of symbiotic nitrogen fixation in some hosts by limiting oxygen diffusion across cell membranes (Vilcheze et al. 1994; Parsons et al. 1987; Abeysekera et al. 1990), from our previous assays, we could not determine whether the poor symbiotic performance of extended hopanoid mutants reflects ineffective nitrogen fixation *per se*, or is simply a consequence of lower general stress resistance. Because we did not observe an extended hopanoid mutant phenotype in soybean, we instead suggested that the extended hopanoid mutant may not survive exposure to nodule cysteine-rich (NCR) peptides, which are synthesized by *A. afraspera* (Czernic et al. 2015) but absent in soybean.

Here, we sought to dissect further the symbiotic phenotypes of *B. diazoefficiens* extended hopanoid mutants in association with *A. afraspera*. We found that the lower nitrogen fixation of extended hopanoid mutants can be fully explained by a reduction in root nodule sizes and rhizobial occupancy, indicating that the underlying defect is unrelated to per-bacteroid nitrogen fixation levels. Using a novel single-nodule tracking approach to quantify *A. afraspera* nodule development, we uncovered both the baseline growth parameters for wild-type nodules and a surprising heterogeneity of extended hopanoid mutant developmental phenotypes. These results challenge the conclusions of our prior study (Kulkarni et al. 2015) and identify new, potentially hopanoid-dependent stages in the *B. diazoefficiens-A. afraspera* symbiosis for future mechanistic work. This work also provides a quantitative reference point for understanding the impact of symbiotically ineffective strains on *A. afraspera* nodule development.

Results

Loss of extended hopanoids results in reduced nodule size

Previously, we observed a symbiotic defect for an extended hopanoid-deficient (Δ*hpnH*) strain of *B. diazoefficiens* in association with *A. afraspera* (Kulkarni et al. 2015). To further validate this defect, we

84 inoculated *A. afraspera* plants with Δ*hpnH* (lacking extended hopanoids), Δ*hpnP* (lacking 2-Me
85 hopanoids), or wild-type *B. diazoefficiens*. At 24 days post-inoculation (dpi), plants inoculated with Δ*hpnH*
86 were shorter than wild type-inoculated plants, although both strains produced equivalent numbers of
87 nodules (Fig. 1b). Δ*hpnH*-inoculated plants also exhibited a roughly 50% decrease in the rate of
88 acetylene gas reduction compared to wild type-inoculated plants at this time point (Fig. 1c). In contrast,
89 the Δ*hpnP* mutant was similar to wild type (Fig. 1b-c). These results are consistent with our previous
90 findings (Kulkarni et al. 2015).
91 To assess Δ*hpnH* viability within *A. afraspera* nodules, we performed morphological analyses of
92 nodules using confocal fluorescent microscopy. Fifty-seven wild-type and 67 Δ*hpnH* nodule cross-
93 sections were stained with a bacterial Live:Dead kit, consisting of the cell-permeable SYTO9 dye (staining
94 all cells) and propidium iodide (PI) (staining only cells with a compromised membrane). We did not
95 observe an increase in predominantly PI-stained nodules for Δ*hpnH* compared to wild type (Fig. 1d; Fig.
96 S1,S2). Signatures of plant necrosis, which we previously associated with Δ*hpnH* when we observed a
97 smaller number of nodules (Kulkarni et al. 2015), occurred prominently in only 1/67 Δ*hpnH* nodules
98 examined (Fig. S2).
99 The most apparent phenotype of Δ*hpnH* nodules was their relatively small size (Fig. S1,S2). We
100 repeated acetylene reduction assays for wild type- and Δ*hpnH*-inoculated plants and then calculated the
101 total nodule dry mass for each plant at 24 dpi. We found a decrease in the nodule dry mass per plant for
102 Δ*hpnH*-inoculated plants that is sufficient to explain the decrease in acetylene reduction rates (Fig. 1e).
103 This result rules out the possibility that nitrogenase functions ineffectively in the absence of extended
104 hopanoids due to inactivation by oxygen, as has been suggested in *Frankia* (Vilcheze et al. 1994;
105 Parsons et al. 1987; Abeysekera et al. 1990), as the per-mg nitrogen fixation rates are not affected by
106 extended hopanoid loss.
107
108 *Δ*hpnH *nodules are more variable in size than wild-type nodules*
109 We next measured acetylene reduction per plant across an extended 40 dpi period, and we
110 observed that the differences in both acetylene reduction rates and nodule dry masses between wild type
111 and Δ*hpnH* steadily decreased with time (Fig. 2a-b). By 40 dpi the overall symbiotic efficiencies of wild

112 type and Δ*hpnH* per plant were indistinguishable, in terms of the plants' qualitative appearance (Fig. 2c-d)
113 as well as their average shoot heights and acetylene reduction rates (Fig. S3). Total nodule counts per
114 plant also did not differ between wild type and Δ*hpnH* at 40 dpi, indicating that the increase in total nodule
115 mass reflects growing nodules rather than more frequent nodulation (Fig. S3).
116 We also measured the radii of individual nodules on ten plants for each strain at 40 dpi (Fig. 2e-f).
117 Interestingly, although *average* nodule sizes did become similar between strains by this time point (0.73
118 vs. 0.88 mm average radii), their underlying distributions were markedly distinct. Wild-type nodule radii
119 appear to form a roughly normal distribution, whereas the Δ*hpnH* nodule radius distribution is bimodal,
120 consisting of a subpopulation of small nodules with small radii (<0.5 mm) that are rarely observed in wild
121 type, as well as a second, larger subpopulation that has a similar median radius as wild type but is
122 skewed towards larger radii (>1.5mm). These data demonstrate that the small-nodule phenotype of
123 Δ*hpnH* persists throughout a 40 dpi time course, but is compensated by greater size heterogeneity, in
124 which a handful of "mega" nodules offset smaller nodules over time.
125
126 *Δ*hpnH *nodule size heterogeneity reflects variable nodule growth rates*
127 To better evaluate the possible origins of the Δ*hpnH* nodule size defect, we studied the kinetics of
128 single nodule development. Beginning one week after inoculation, we collected images of entire plant
129 roots every 3-5 days up to ~40 days post-inoculation (Fig. S4,S5). From these images, we identified
130 nodules that were clearly visible (*e.g.* not obscured by lateral roots or more recently emerged nodules) in
131 at least five time points (Fig. 3a) and measured their radii. We then calculated nodule volumes by
132 approximating nodules as spheres and plotted the volume of the tracked nodules over time. While we
133 again observed that many Δ*hpnH* nodules were smaller at 40 dpi than any of the wild type nodules, we
134 also found that nodule growth was highly variable both within and between strains (Fig. 3b-c).
135 We then developed a simple framework for quantifying nodule development, in which nodule
136 growth is defined by the following variables: the time (t_i) of the initial intracellular infection event and the
137 volume of the nascent nodule (V_i), equivalent to the volume of one infected *A. afraspera* cortical cell; the
138 time (t_{min}) and volume (V_{min}) at which a clearly visible, spherical nodule has developed; the rate of growth
139 of a nodule once it has become visible (dV/dt); and the time (t_{max}) and volume (V_{max}) of a nodule when its

growth has stopped (Fig. 3d). To calculate these variables, we fit each nodule's growth over time to three different growth models: exponential, quadratic, and a generalized logistic (*e.g.* sigmoidal) equation commonly used for plant growth (Szparaga and Kocira 2018; Richards 1959) (see Methods for complete details). Sigmoidal models generally provided the best fit to the experimental data, so these models were used for growth parameter calculation (Fig. 3e; Fig. S6, S7).

The growth rates of Δ*hpnH* nodules were lower on average than wild-type nodules (Fig. 3f), with roughly a third of tracked nodules exhibiting growth rates lower than observed for wild type (<0.1 mm^3/dpi). A similar fraction of nodules had smaller final volumes than wild type (Fig. 3g). We further found that the growth rate of a nodule and its maximum size are positively linearly correlated for both strains, with Pearson coefficients of ~0.64 ($p<10^{-9}$) for wild type and ~0.75 ($p<10^{-15}$) for Δ*hpnH,* and that the subpopulation of nodules with lower-than-wild-type growth rates and small nodule sizes are the same (Fig. 3h). We interpret these data to suggest that host proliferation is slower in a subset of nodules infected with Δ*hpnH*, and that this largely accounts for the low final volume of these nodules.

We also noted that Δ*hpnH* nodule sizes at 40 dpi differed between these single-nodule volume measurements (Fig. 3g) and our previous 40 dpi end-point measurements of nodule radii (Fig. 2e), in that we did not observe larger-than-wild-type "mega" nodules in the single-nodule dataset. This discrepancy likely reflects the smaller sample size in our single-nodule tracking experiments (84 compared to 268 end-point nodules), and the low frequency of "mega" nodule formation. To verify this, we selected 10,000 random subsets of 84 nodules from the 268 Δ*hpnH* nodules shown in Figure 2e, converted the nodule radii to volumes, and found that there is no statistically significant difference ($p<0.05$) between a random subset of Fig. 2e and the Δ*hpnH* single-nodule tracking data in ~92% (9184/10000) of cases. Thus the differences in nodule size distributions in Figure 3g and Figure 2e are consistent with sampling error.

We also calculated each nodule's window of maximum growth, defined as the time required for a nodule to increase from 10% to 90% of its final volume. Neither the time at which a nodule reaches 90% of its maximum volume, t_{max}, nor the window of maximum growth differs significantly between Δ*hpnH* and wild type (Fig. S8a-b). The window of maximum growth for each nodule is also uncorrelated with their final volume or growth rate, indicating that small nodules are not prematurely aborted; rather, their growth periods are similar to larger nodules (Fig. S9a-d).

168 To better understand the subpopulation of small, slow-growing Δ*hpnH* nodules, we isolated
169 nodules with <0.5 mm radius, sectioned and stained them with SYTO9, PI and Calcofluor, and imaged
170 them with confocal microscopy. We found that while most small Δ*hpnH* nodules contained a single,
171 continuous infection zone, a large fraction were un- or under-infected with bacteria, often exhibiting
172 disorganized central infection zones (~37%; 28/75) (Fig. 4a; Fig. S10). Of the fully infected small Δ*hpnH*
173 nodules, a subset contained primarily PI-stained, likely dead bacterial cells (~25%; 12/47) (Fig. 4a; Fig.
174 S10). Similar proportions of under-infected nodules or nodules primarily occupied with membrane-
175 compromised bacteria did not occur in larger Δ*hpnH* nodules harvested at the same time point, although
176 fragmented infection zones were still common (Fig. 4b; Fig. S11). We also compared the subpopulation of
177 small Δ*hpnH* nodules at 40 dpi to two wild-type nodule populations: similarly small nodules harvested at
178 10 and 25 dpi (Fig. 4a; Fig S12; Fig. S13), and nodules harvested at the same 40 dpi time point (Fig. 4b;
179 Fig. S14). Again, we found that high proportions of under-infected nodules and membrane-compromised
180 bacteria were unique to the Δ*hpnH* small-nodule subset.
181
182 *Δ*hpnH *nodule emergence is delayed*
183 The "true" beginning of nodule formation is the time when the first *A. afraspera* cortical cell is
184 infected, t_i (Fig. 3d). However, this initial infection event is not visible at the root surface, and it is difficult
185 to extrapolate from sigmoidal models in which the growth curves approach the initial volume $V_i \sim 0$ mm^3
186 asymptotically. As a proxy for t_i, we defined three alternate t_{min} as the times at which nodules reached
187 three arbitrarily small volumes: V = 0.05 mm^3, V = 0.1 mm^3, and V = 0.2 mm^3. When t_{min} is defined by V =
188 0.05 mm^3 or 0.1 mm^3, t_{min} could not be accurately calculated for all nodules, as the sigmoidal models
189 sometimes predicted an impossible $t_{min} < 0$ (Fig. S8c). These nodule volumes are also too small to be
190 seen on the root surface, and we had no experimental means to determine the accuracy of the
191 calculations in this low-volume regime. When t_{min} is defined by V = 0.2 mm^3 (the smallest nodule volume
192 that we could identify in our single-nodule tracking assays), there is a small but statistically significant
193 increase for Δ*hpnH* relative to wild type (Fig. S8c).
194 To independently verify this delay in nodule emergence, we inspected the roots of 20 wild type-
195 and 20 Δ*hpnH*-inoculated plants over 40 dpi and recorded the number of visible nodules per plant each

196 day. We found a more even distribution of observed t_{min} for Δ*hpnH* relative to wild type, with a 1-3 day
197 shift in the most frequent dpi. Surprisingly, we also found that the formation of new nodules is periodic,
198 with a new "burst" of nodules emerging roughly every 18 days (Fig. 3i). This periodicity of nodule
199 emergence appears to be similar between strains.

200 While the slight t_{min} delay for Δ*hpnH* is consistent with longer times required to initiate the
201 symbiosis (*e.g.* root surface colonization, invasion of the root epidermis and cortex, and intracellular
202 uptake), it is also possible that a delay in t_{min} simply reflects a lower rate of nodule growth immediately
203 after the first intracellular infection. To address this, we compared the calculated value of t_{min} (defined by
204 $V = 0.2\ mm^3$) to the maximum growth rates and volumes for each nodule (Fig. S9e-f). We did not find that
205 nodules with lower growth rates and final volumes than wild type were more likely to have a later t_{min},
206 supporting the interpretation that the delay in t_{min} of Δ*hpnH* could be due to a separate initiation defect.
207 Interestingly, t_{min} is also not correlated with the period in which maximum nodule growth occurs, such that
208 later-emerging nodules have similar growth period to nodules formed within a few dpi (Fig. S9g-h). This
209 indicates that although nodule emergence is restricted to narrow, periodic windows (Fig. 3i), once a
210 nodule has entered its maximum growth phase, its continued growth is comparatively unconstrained.
211

212 *Δ*hpnH *is delayed in a pre-endosymbiont stage*

213 We next performed competition assays using a standard fluorescence labeling approach. We first
214 generated Δ*hpnH* and wild-type strains expressing chromosomally-integrated fluorescent proteins, and
215 then we co-inoculated *A. afraspera* with different ratios of these two strains. As control experiments, we
216 also co-inoculated each tagged strain with its untagged counterpart, in order to determine the effect of
217 fluorescent protein overexpression on each strain's competitiveness. After 40 dpi we measured the size
218 of nodules on plants inoculated with each strain combination and ratio, then sectioned and fixed nodules
219 for imaging. Although we expected each nodule to contain a clonal population of symbionts based on
220 previous work (Bonaldi et al. 2011; Ledermann et al. 2015), the majority of nodules instead contained a
221 mixture of both strains (Fig. 5a).

222 We quantified the relative abundance of each strain in each nodule by fluorescence imaging; in
223 our control experiments, in which only one fluorophore-expressing strain was present, a DNA dye was

224 used to label all bacteria. Both WT-YFP and Δ*hpnH*-mCherry were significantly out-competed by their
225 corresponding untagged strains, with higher proportions of tagged strains correlating with lower bacterial
226 DNA abundance and smaller nodule and/or infection zone sizes (Fig. 5b-c; Fig. S16-S18). Additionally,
227 plants co-inoculated with untagged-Δ*hpnH* and Δ*hpnH*-mCherry were significantly shorter than plants
228 inoculated with untagged-Δ*hpnH* only, suggesting Δ*hpnH*-mCherry is symbiotically defective (Fig. S15).
229 These effects of fluorophore overexpression made it difficult to interpret our WT-YFP and Δ*hpnH*-
230 mCherry competition data, so we developed an alternative, antibiotics-based method to study the timing
231 of early symbiotic initiation. First, we identified antibiotics that were effective against *B. diazoefficiens* but
232 would minimally affect *A. afraspera* growth. We tested three antibiotics (100 µg/ml streptomycin, 100
233 µg/ml kanamycin, and 20 µg/ml tetracycline) and treated non-inoculated plants with these antibiotics for
234 two weeks, alone and in combination. After this treatment, we found that neither kanamycin nor
235 streptomycin, nor the combination of the two, significantly affected plant appearance, shoot height, or root
236 and shoot dry masses compared to untreated controls (Fig. S19). Plants treated with tetracycline were
237 noticeably more yellow in color, indicating chlorosis, and the roots and plant medium became brown;
238 these plants also had lower shoot and root dry masses than untreated plants (Fig. S19).
239 Next, because the Δ*hpnH* strain is more sensitive to antibiotics than wild type (Kulkarni et al.
240 2015), we tested various concentrations of the non-plant-perturbing antibiotics streptomycin and
241 kanamycin to identify concentrations that would result in the same rates of cell death for both strains. We
242 inoculated plant growth media with wild type or Δ*hpnH* to the same cell densities and under the same
243 environmental conditions as in plant inoculation experiments. The wild-type culture was supplemented
244 with 100 µg/ml streptomycin plus 100 µg/ml kanamycin, and Δ*hpnH* cultures were supplemented with
245 decreasing concentrations of these antibiotics: 75, 50 and 25 µg/mL each. Samples of the cultures were
246 then collected, serially diluted and added to PSY plates to estimate colony-forming units (cfus) per mL
247 over time. At 50 µg/mL kanamycin plus 50 µg/mL streptomycin, the rate of decrease in cfus/mL for Δ*hpnH*
248 was equivalent to that of wild type treated with 100 µg/ml kanamycin plus streptomycin (Fig. 5d).
249 Finally, we inoculated 40 plants each with wild type or Δ*hpnH* and added streptomycin or
250 kanamycin to 100 µg/mL each or 50 µg/mL each, respectively, at various points post-inoculation. After 40
251 days we counted the number of nodules per plant, and found that antibiotics were able to block nodule

252 formation over a ~50% longer window in Δ*hpnH* compared to wild type (Fig. 5e). The decrease in nodules
253 formed at different antibiotic treatment time points was also evident in the overall appearance of the
254 plants (Fig. 5f). These results suggest that Δ*hpnH* requires more time on average to reach the
255 intracellular stage of the symbiosis, at which point we presume that the bacteria are protected from
256 antibiotic by the host cells. These data are consistent with Δ*hpnH* requiring more time to colonize the root
257 surface, invade the root epidermis, and/or be internalized by host cells.
258
259 *Extended hopanoids support surface attachment and motility* in vitro
260 Because we found that expression of genetic tags in wild type and Δ*hpnH* perturbed their
261 symbiosis with *A. afraspera,* and because we found that the hopanoid mutant viability is reduced by
262 sonication, centrifugation, and mechanical or detergent-based tissue disruption techniques required to re-
263 isolate bacteria from plants, we could not confidently follow these strains *in planta*. Instead, we used an *in*
264 *vitro* approach to study two steps in the initiation of the symbiosis: (1) bacterial motility toward or along
265 the *A. afraspera* root, and (2) stable attachment of bacteria to the root surface (Wheatley and Poole
266 2018). To determine whether Δ*hpnH* is less motile than wild type, we inoculated low-agar, PSY plates
267 with Δ*hpnH* or wild type and measured the rate of zone of swimming over time. We observed that
268 diameter of motility was reduced in Δ*hpnH* compared to wild type (Fig. 6a-b), consistent with a swimming
269 motility defect; however, because we have previously shown that Δ*hpnH* grows more slowly in this
270 medium than wild type (Kulkarni et al. 2015), we could not rule out the possibility that slower zone
271 expansion simply reflects a longer doubling time.
272 To investigate the nature of the plate motility defect, we studied the motility of single *B.*
273 *diazoefficiens* cells. We inoculated cells into a glass-bottom, sterile PSY flow cells with 100μL of each
274 strain and recorded the movement of cells near the glass surface at 5 ms time resolution. Trajectories of
275 individual swimming cells, defined as having super-diffusive motion and a trajectory radius of gyration
276 >2.5 μm, were calculated and analyzed in MATLAB (Lee et al. 2018). In agreement with our low-agar
277 swimming plates, we found significantly fewer ($p < 0.0001$) motile cells for Δ*hpnH* (N = 65 ± 29) than wild
278 type (N= 368 ± 60) in PSY medium (Fig. 6c; Table S1). The average mean-speed among motile cells
279 were similar between strains: $\langle V \rangle_{\Delta hpnH}$ = 24.83 ± 7.0 μm/sec and $\langle V \rangle_{wt}$ = 22.75 ± 6.7 μm/sec (Fig. 6d;

280 Table S1). Because the composition of PSY differs greatly from that of the plant growth medium (BNM),
281 we repeated these assays in BNM supplemented with arabinose. Under this condition, we again
282 observed a lower fraction of motile Δ*hpnH* cells than wild type ($N_{\Delta hpnH}$ = 54 ± 59, N_{wt}= 450 ± 310) with
283 similar mean speeds between strains (Fig. 6e-f; Table S1).

284 We next tested the surface attachment capabilities of Δ*hpnH* and wild type by incubating dense
285 bacterial cultures on glass coverslips and quantifying the fraction of the surface covered with stably
286 adherent cells after two hours. In PSY medium, both strains adhered poorly, and there was no significant
287 difference in their attachment efficiencies (Fig 6g; Fig. S20). In BNM supplemented with arabinose, both
288 strains adhered to glass better than in PSY, and Δ*hpnH* attachment levels were significantly lower than
289 wild type (Fig. 6g; Fig. S20). The decreased adhesion and reduced motile cell population of Δ*hpnH*
290 suggest that stable root colonization by this strain may be less efficient.

291 **Discussion**

292 Hopanoids are well-established mediators of bacterial survival under stress, and previously we
293 showed that the capacity for hopanoid production is enriched in plant-associated environments (Ricci et
294 al. 2014) and required for optimal *Bradyrhizobia-Aeschynomene* spp. symbioses (Silipo et al. 2014;
295 Kulkarni et al. 2015). Here we performed a detailed, quantitative evaluation of the extended hopanoid
296 phenotypes in the *Bradyrhizobium diazoefficiens-Aeschynomene afraspera* symbiosis. We determined
297 that extended hopanoid mutants fix nitrogen at similar rates as wild type on a per-bacteroid level,
298 demonstrating that in this host, extended hopanoids are not required to protect nitrogenase from oxygen,
299 as often has been speculated (reviewed in Belin et al. 2018). Instead, we found that the extended
300 hopanoid mutants' lower *in planta* productivity can be fully attributed to changes in the kinetics of nodule
301 development. By tracking the development of individual root nodules, we observed later nodule
302 emergence times in Δ*hpnH*-inoculated plants. *In vitro*, Δ*hpnH* cells adhered poorly to glass and were less
303 motile than wild type, suggesting they may colonize roots less efficiently (Fig. 7a-b). A third of Δ*hpnH*
304 nodules also grew significantly slower than wild type and were smaller at maturity. Many of these small
305 nodules contained low symbiont densities; a subset of larger Δ*hpnH* nodules also had lower symbiont
306 loads, due to infection zone fragmentation. The origin of this under-infection is unclear. It is possible that
307 bacteria are inefficiently internalized or retained, and this phenotype is simply propagated as nodules

308 develop (Fig. 7c-d). Alternatively, low symbiont densities may reflect symbiont degradation in a previously
309 fully infected nodule (Fig. 7e).

310 These observations challenge two conclusions from our previous work, requiring a refinement of
311 our interpretation of the roles of extended hopanoids in the plant context (Kulkarni et al. 2015). First, we
312 reported that there was no symbiotic defect of the Δ*hpnH* strain in soybean, based on the observation
313 that nitrogen fixation per mg nodule dry weight was similar to wild type. Given that this study revealed that
314 a reduction in nodule dry weight explains the Δ*hpnH* defect in *A. afraspera*, it is possible that this strain is
315 also defective in its native host, but this defect was obscured by differences in normalization between the
316 soybean and *A. afraspera* datasets. Second, the majority of Δ*hpnH* nodules had wild type-like growth
317 kinetics and morphologies, with a few "mega" nodules displaying unusually fast growth. This finding
318 appears inconsistent with an inability to survive NCR peptides, unless NCR peptide expression levels are
319 extremely variable, or if the mechanisms that compensate for extended hopanoid loss are inconsistent.

320 What other mechanisms might underpin these extended hopanoid mutant phenotypes? Perhaps
321 they are simply consequences of less rigid *B. diazoefficiens* membranes. The fraction of motile cells in *E.*
322 *coli* populations has been suggested to be sensitive to changes to the mechanical properties of the outer
323 membrane (Gupta et al. 2006), and membrane-based mechanotransduction is required by diverse
324 bacteria to stimulate extracellular matrix production and cement their attachment to surfaces (Petrova and
325 Sauer 2012; Persat 2017). *B. diazoefficiens* mutants with weakened cell walls also have been shown to
326 be deficient in symbiosis with *A. afraspera* through an NCR peptide-independent mechanism (Barriere et
327 al. 2017), which may be elicited by Δ*hpnH*. Extended hopanoid loss may also have secondary effects on
328 *Bradyrhizobium-Aeschynomene* signaling. In the *Frankia*-actinorhizal symbiosis, bacterial extended
329 hopanoids can contain the auxinomimetic compound phenyl-acetic acid (PAA) (Hammad et al. 2003), and
330 though the effects of hopanoid loss on the bacterial metabolome have not been examined, changes in
331 hopanoid production may impact the synthesis and/or secretion of symbiotically active compounds.
332 Future work will be required to determine whether changes in signaling or membrane mechanics
333 dominate the hopanoid mutant phenotypes, and at which developmental stages.

334 Regardless of the underlying mechanism, it is curious that the absence of extended hopanoids is
335 not a death knell for the *B. diazoefficiens-A. afraspera* symbiosis at any stage. In our *in vitro* studies,

336 mean speeds among motile Δ*hpnH* cells were indistinguishable from wild type, and though we cannot
337 rule out more subtle defects in the direction of movement or chemotaxis, this suggests that motility
338 systems of Δ*hpnH* cells function properly once induced. Similarly *in planta*, Δ*hpnH* nodules developing at
339 wild-type rates and reaching average wild-type volumes did occur – and, in the case of "mega" nodules,
340 some exceeded their wild-type counterparts.

341 Why do Δ*hpnH* populations form two distinct populations (wild-type-like or defective) rather than
342 falling on a continuous distribution of behavior? Bimodality can reflect switch-like, or threshold-based,
343 regulation, and perhaps in the Δ*hpnH* strain, a fraction of cells cannot support levels of signaling above
344 the threshold required for proper function. Nodules may also differ in the extent to which extended
345 hopanoid loss is compensated. In *Methylobacterium extorquens* and *Rhodopseudomonas palustris*
346 (Bradley et al. 2017; Neubauer et al. 2015), hopanoid loss results in upregulation of other membrane-
347 rigidifying lipids including carotenoids and cardiolipins, and in other plant-microbe systems, lipid exchange
348 between hosts and microbes has been observed (Keymer 2018), suggesting that Δ*hpnH* nodule
349 phenotypes may relate to the local availability of structurally or functionally similar metabolites. Because
350 of these diverse possible explanations for Δ*hpnH* heterogeneity, a detailed comparison of wild type-like
351 and defective nodules, including the distributions of lipids and other metabolites, bacteroid morphology
352 and penetrance, and gene expression variability, will be required to determine why some Δ*hpnH* nodules
353 succeed and others do not.

354 Beyond hopanoids, our results provide insight into the developmental control of nodule formation
355 by *A. afraspera* hosts. We find that nodulation occurs in bursts separated by fixed 18-day intervals, and
356 that the timing of these bursts is unrelated to net fixed nitrogen production across the root, more likely
357 reflecting the inherent dynamics of the underlying signaling networks. The growth period of individual
358 nodules is similarly deterministic, suggesting that *A. afraspera* hosts do not respond to ineffective
359 symbionts by prematurely aborting nodule development. Rather, we find that *A. afraspera* nodules can be
360 primarily distinguished by their growth rates, *e.g.* the frequencies of infected host cell division. This finding
361 suggests that in *A. afraspera* host cell mitosis and symbiont performance may be coupled, enabling future
362 studies on the molecular signals through which this coupling occurs.

363 Finally, our results underscore the importance of identifying the most informative, least perturbing
364 tools for interrogating legume-microbe symbiosis. Employing quantitative, time-resolved, single-nodule
365 and single-cell approaches rather than bulk measurements were essential for uncovering the diverse
366 phenotypes of the *B. diazoefficiens* extended hopanoid mutants and yielded unexpected information on
367 regulation of nodule development by *A. afraspera*. We have also shown the limitations of introducing
368 overexpressed genetic tags into bacteria. While use of these tags has undoubtedly enhanced our
369 understanding of legume-microbe symbiosis (Ledermann et al. 2018), they may not fully capture the
370 behavior of native organisms. Additionally, our work is one of many to emphasize the importance of
371 appropriate culture models for mimicking the host environment, as the Δ*hpnH* surface attachment defect
372 was observed in plant growth medium but not in a standard richer medium. A more detailed analysis of
373 the host environment, including the full milieu of root exudates (Sugiyama and Yazaki 2012), available
374 carbon sources (Pini et al. 2017) and trace metals specific to each legume, will improve *in vitro* models of
375 legume-bacteria interactions and may allow selection of strains with improved performance in agriculture.
376

377 **Methods**

378 B. diazoefficiens *culture and strain generation*

379 *B. diazoefficiens* hopanoid biosynthesis mutants were generated previously (Kulkarni et al. 2015).
380 For construction of YFP- and mCherry-expressing strains, fluorophore expression vectors pRJPaph-YFP
381 and pRJPaph-mCherry (Ledermann et al. 2015) were provided as a gift from Prof. Dr. Hans-Martin
382 Fischer (ETH Zurich). These vectors were introduced into *B. diazoefficiens* by conjugation with the β2155
383 DAP auxotroph strain of *E.coli*, using the following protocol: *B. diazoefficiens* wild type and Δ*hpnH* were
384 grown in 5 mL PSY medium(Regensburger and Hennecke 1983) at 30°C and 250 rpm to an OD_{600} of
385 ~1.0 (wild type) or of 0.5-0.8 (Δ*hpnH*). β2155 strains carrying pRJPaph vectors were grown to an OD_{600} of
386 0.5-0.8 in 5 mL LB supplemented with 10 µg/mL tetracycline and 300 µm DAP at 37°C and 250 rpm. Both
387 *B. diazoefficiens* and β2155 donor cultures were pelleted at 3250 x g for 30 minutes, washed three times
388 in 0.9% sterile saline, and resuspended in 0.9% sterile saline to a final OD_{600} of 1.0. *B. diazoefficiens*
389 strains and β2155 donor cells were combined at a 4:1 ratio, respectively, and mixed by repeated
390 pipetting. Aliquots (50 µl) of these 4:1 mixtures were dropped to PSY plates supplemented with 300 µm

391 DAP, dried in a biosafety cabinet, and incubated for 48 hours at 30°C. Conjugation pastes were then
392 removed from plates and resuspended in 5 mL sterile saline, pelleted at 3250 x g for 30 minutes and
393 washed twice, in order to remove residual DAP. Washed cells were pelleted a final time and resuspended
394 to 200 µl in 0.9% sterile saline and plated onto PSY plates supplemented with 20 µg/mL (wild type) or 10
395 µg/mL (Δ*hpnH*) tetracycline. Colonies appeared after 7-10 days (wild type) or 10-14 days (Δ*hpnH*) and
396 were streaked onto fresh PSY/tetracycline plates, then screened for fluorescence using a Lumascope 720
397 fluorescent microscope (Etaluma). Fluorescent colonies were then sequenced to verify insertion of the
398 pRJPaph vectors into the *scoI* locus.
399
400 A. afraspera *cultivation and inoculation with* B. diazoefficiens
401 *A. afraspera* seeds were obtained as a gift from the laboratory of Dr. Eric Giraud (LSTM/Cirad,
402 Montpelier, France). Seeds were sterilized and scarified by incubation in 95% sulfuric acid at RT for 45
403 minutes, followed by 5 washes in sterile-filtered nanopure water and a second incubation in 95% ethanol
404 for 5 minutes at RT. After ethanol treatment seeds were washed 5X and incubated overnight in sterile-
405 filtered nanopure water. Seeds were then transferred to freshly poured water/agar plates using sterile,
406 single-use forceps in a biosafety cabinet, and germinated for 24-72 hours in the dark at 28-32°C.
407 Seedlings were then placed in clear glass test tubes containing 100 mL of sterile, nitrogen-free
408 Buffered Nodulation Medium (BNM)(Ehrhardt et al. 1992) and grown for 7-10 days in plant growth
409 chambers (Percival) under the following settings: 28°C, 80-90% humidity, and 16 hour photoperiod under
410 photosynthetic light bulbs (General Electric) emitting ~4000 lumens/ft^2. In parallel, *B. diazoefficiens*
411 strains were grown in 5-10 mL PSY liquid culture at 30°C and 250 rpm to stationary phase (OD_{600} > 1.4).
412 Stationary phase cultures were diluted into PSY one day prior to plant inoculation to reach an OD_{600} of
413 ~0.8 at the time of inoculation. OD_{600} ~ 0.8 cultures were pelleted at 3250 x g for 30 minutes at RT,
414 washed once in PSY, then resuspended in PSY to a final OD_{600} of 1.0. Resuspended *B. diazoefficiens*
415 cultures were directly inoculated into the plant medium in a sterile biosafety cabinet; 1 mL of OD_{600}=1.0
416 culture was added per plant. Inoculated plants were then returned to growth chambers and maintained for
417 the times indicated for each experiment. For longer experiments (lasting longer than ~30 days post-
418 inoculation), plant growth tubes were refilled with sterile-filered nanopure water as needed. To minimize

419 cross-contamination, inoculated plants and non-inoculated plants were cultivated in separate growth
420 chambers, and growth chambers were sterilized with 70% ethanol followed by UV irradiation for at least
421 24 hours between experiments.
422
423 *Acetylene reduction experiments*
424 Individual plants were transferred to clear glass 150 mL Balch-type anaerobic culture bottles containing
425 15 mL BNM medium and sealed under a gas-tight septum. After sealing, 15 mL of headspace gas (10%
426 of the culture bottle volume) was removed and replaced with 15 mL of acetylene gas (Airgas). Plants in
427 culture bottles were incubated in the light at 28°C in growth chambers for 3-6 hours. A 100 µl sample of
428 the headspace gas was removed using a gas-tight syringe (Hamilton), and this sample was injected and
429 analyzed for ethylene signal intensities using a Hewlett Packard 5890 Series II GC with Hewlett Packard
430 5972 Mass Spectrometer with a 30mx0.320mm GasPro Column (Agilent Technologies) and a 2 mm ID
431 splitless liner (Restek Corporation). Following acetylene reduction measurements, plants were removed
432 from jars and plant shoot heights and number of nodules per plant were recorded. When nodule dry mass
433 measurements were performed, nodules were harvested with a razor blade, transferred into pre-weighed
434 Eppendorf tubes, dried at 50°C for a minimum of 48 hours, then weighed again.
435
436 *Live:Dead staining and imaging of nodule cross-sections*
437 Nodules were hand-sectioned with razor blades and immediately transferred into a fresh solution
438 of 5 µM SYTO9 (diluted 1:100 from a 500 uM stock in DMSO at -20°C; Thermo Fisher) and 0.02 mg/mL
439 (30 µM) propidium iodide (diluted 1:50 from a 1 mg/mL stock stored in water at 4°C; Thermo Fisher) in
440 PBS. Nodule sections were incubated in this SYTO9/propidium iodide solution at room temperature for 30
441 minutes in the dark with gentle shaking, washed 5X in PBS, and fixed in 4% paraformaldehyde (Electron
442 Microscopy Sciences) in PBS overnight in the dark at 4°C. Fixed sections were washed 5X in PBS and
443 transferred to a freshly prepared solution of 0.1 mg/mL Calcofluor White (Fluorescence Brightener 28;
444 Sigma) in PBS. The sections were incubated in the Calcofluor solution in the dark for 1 hour at RT with
445 gentle shaking and washed 5X in PBS to remove excess dye.

446 Prior to imaging, sections were transferred to 30 mm imaging dishes with 20 mm, #0 coverglass
447 bottoms (MatTek) and overlaid with sterile 50% glycerol. Nodule images were collected on a Leica TCS
448 SPE laser-scanning confocal (model DMI4000B-CS) using a 10X/0.3 NA APO ACS objective and solid-
449 state laser lines for fluorophore excitation at the following settings for each dye: Calcofluor, 405 nm
450 excitation/410-500 nm emission; SYTO9, 488 nm excitation/510-570 nm emission; PI, 532 nm
451 excitation/600-650 nm emission. These images were then processed to enhance brightness and contrast
452 in FIJI(Schindelin et al. 2012; Schneider et al. 2012).
453
454 *Nodule diameter and volume measurements*
455 Inoculated *A. afraspera* root nodules were imaging using a high-definition Keyence VHX-600
456 digital microscope at 20X magnification. For end-point root nodule volume measurements at 40 days
457 post-inoculation, plants were removed from the growth chamber and imaged at RT on paper towels, then
458 discarded. Nodule diameters were measured using the line tool in FIJI and recorded using a custom FIJI
459 macro. For tracking nodule volumes over time, plants were serially removed from their growth chambers
460 and transferred to a plastic dish containing 150 mL of sterile BNM pre-warmed to 28°C. Images of
461 sections of the plant root were collected serially from the hypocotyl to the root tip. Following collection of
462 images, plants were immediately returned to their original growth tubes in the growth chamber. Plastic
463 dishes were sterilized for 10 minutes in 10% bleach, washed three times in sterile-filtered nanopure
464 water, sprayed with 70% ethanol/water, and air-dried before each new plant was imaged. A fresh aliquot
465 of sterile, pre-warmed BNM also was used for each plant. After the time course was completed, images of
466 entire plant root systems were reconstructed by eye for each plant at each time point. For nodules
467 appearing in at least five time points, nodule diameters were measured as described for the end-point
468 measurements and were converted to approximate volumes in R using the equation $V = 4/3\pi r^3$.
469
470 *Nodule growth curve fitting and analysis*
471 All analyses of nodule growth, and corresponding plots, were generated in R. For nodule growth
472 curve fitting, three model equations were used to identify the best fit, as follows:
473

(1) exponential function:

$$V = \boldsymbol{a}e^{-\boldsymbol{b}t} + \boldsymbol{c}$$

(2) quadratic function:

$$V = \boldsymbol{a}t^2 + \boldsymbol{b}t + \boldsymbol{c}$$

(3) generalized logistic function (expressed as a Richard's function with a time shift):

$$V = \frac{\boldsymbol{a}}{(1 + e^{-\boldsymbol{b}(t-\boldsymbol{c})})^{(\frac{1}{\boldsymbol{d}})}}$$

Calculation of the optimal parameter values for each equation (e.g. the values of **a**, **b**, **c**, and **d**) and the standard error for each curve compared to the raw data were performed using the built-in function *nlm*() in R. In some cases, *nlm()* could not produce a best-fit model without specifying initial values for the function parameters. For exponential models, an equation of best fit could be successfully determined without specification of initial values for parameters **a**, **b** and **c**. For quadratic models, initial parameter values were required and were set to **a**=0, **b**=10 and **c**=0 for each nodule plot, after identifying these initial parameter values as broadly optimal based on an initial parameter sweep of -50 to 50 for each plot. For sigmoidal models, no broadly optimal initial values could be identified, so a parameter sweep was performed for each plot with the initial value of **a** set to the maximum observed nodule volume (as **a** describes the upper asymptote of the sigmoidal curve), **b** ranging from 0.1 to 1, **c** ranging from 0 to 10, and **d** ranging from 0.01 to 1.0. In the sigmoidal plots, an initial point of (0,0) was added to the nodule volume time series to improve fitting.

Because the sigmoidal model provided the best fits, extrapolation of nodule growth characteristics was performed on sigmoidal models only. The maximum nodule volume, $\mathbf{V_{max}}$, is defined as the upper asymptote of the sigmoidal growth curve, *e.g.* **a**. The nodule initiation time, $\mathbf{t_{min}}$, was defined in three separate ways: the times at which the nodule volume is equal to 0.05, 0.1, or 0.2 mm^3 (*e.g.* through solving 0.05, 0.1, or 0.2 = $\mathbf{a}/((1+e^{(-\mathbf{b}(t-\mathbf{c}))})^{(1/\mathbf{d})})$ for *t*). The maximum nodule growth rate, **dV/d*t***, was defined

498 as the average rate of growth (*e.g.* slope) between the time at which the volume is 10% of $\mathbf{V_{max}}$ and the
499 time at which the volume is 90% of $\mathbf{V_{max}}$. The time at which each nodule reaches its maximum size, $\mathbf{t_{max}}$,
500 was approximated as the time at which the volume is 90% of $\mathbf{V_{max}}$, since the "true" maximum volume is
501 asymptotic to the growth curve and is therefore never fully reached in the model.
502
503 *Competition assays*
504 mCherry-tagged Δ*hpnH* and YFP-tagged wild type *B. diazoefficiens* were grown to stationary
505 phase (OD_{600} > 1.4) in 10 mL PSY cultures supplemented with 20 µg/mL (wild type) or 10 µg/mL (Δ*hpnH*)
506 tetracycline; untagged strains were grown in PSY. On the day prior to inoculation, all strains were diluted
507 into 50-150 mL tetracycline-free PSY to reach an OD_{600} of ~0.8 at the time of inoculation. *A. afraspera*
508 plants were cultivated pre-inoculation in test tubes as described above, with the addition of covering the
509 growth tubes in foil to minimize the production of chlorophyll in the plant roots, which spectrally overlaps
510 with mCherry. At the time of inoculation, all cultures were pelleted at 3250 x g for 30 minutes at RT,
511 washed three times, then resuspended in PSY to a final OD_{600} of 1.0. A 10 mL culture of each strain ratio
512 for inoculation was generated a sterile 15mL Falcon tube; for example, for a 50:50 mixture of mCherry-
513 tagged Δ*hpnH* and YFP-tagged wild type, 5 mL of each strain was combined. These cultures were mixed
514 thoroughly by gentle pipetting, and 1 mL of the mixtures was added to directly to the plant medium for 7-8
515 plants per strain mixture.
516 After 45-60 days, plants were harvested. First, plant heights and the number of nodules per plant
517 were recorded. Then, the roots were cut from the stem and images of all nodules for each plant were
518 collected on a high-definition Keyence VHX-600 digital microscope at 20X magnification. These nodules
519 were then cross-sectioned and immediately transferred to Eppendorfs containing 4% paraformaldehyde
520 (Electron Microscopy Sciences) in PBS. Fresh sections were fixed overnight in the dark at 4°C, washed
521 5X in PBS, and stored in PBS supplemented with 0.1% azide in the dark at 4°C until imaging.
522 Fixed sections were stained in Calcofluor (all strain combinations), SYTO9 (WT-YFP and WT co-
523 inoculation only) or propidium iodide (mCherry-Δ*hpnH* and Δ*hpnH* co-inoculation only) as described for
524 Live:Dead staining. Imaging was performed as described for Live:Dead staining using a 5X objective.
525 Given the high autofluorescence of these nodules and low mCherry and YFP signal intensities, the

526 following excitation/emission settings were used: Calcofluor, 405 nm excitation/410-460 nm emission;
527 YFP/SYTO9, 488 nm excitation/500-550 nm emisasion; mCherry, 532 nm excitation/600-650 nm
528 emission.

529 Quantification of nodule statistics (including nodule and infection zone areas, signal intensity of
530 YFP, mCherry, SYTO9 and propidium iodide) was performed on raw images using a custom FIJI macro.
531 Briefly, nodule images were opened at random, infection zones (IZs) and whole nodules were circled by
532 hand and saved as discrete regions of interest (ROIs), and the area and intensity in each channel were
533 measured automatically for all ROIs. These measurements were exported as a text table and various
534 parameters from these measurements were calculated using custom Python scripts, as indicated in the
535 Results. Plots of all parameters and statistical comparisons were generated using custom R scripts.
536

537 *Antibiotic treatment of inoculated plants*

538 *A. afraspera* plants were cultivated as described above and the following antibiotics were added
539 to non-inoculated plants 7 days after rooting in 100 mL BNM growth tubes: kanamycin to 100 µg/mL,
540 streptomycin to 100 µg/mL, tetracycline to 20 µg/mL, kanamycin plus tetracycline, kanamycin plus
541 streptomycin, streptomycin plus tetracycline. Plants were grown in antibiotics under normal plant growth
542 conditions for 14 days, after which plants were visually inspected. Plant heights were also recorded, and
543 the root and shoot systems were separated with a razor blade, transferred into pre-weighed 15 mL Falcon
544 tubes, dried at 50°C for a minimum of 48 hours, then weighed again.

545 Antibiotic treatments of Δ*hpnH* and wild-type *B. diazoefficiens* were performed by growing
546 antibiotic 5 mL PSY cultures of each strain to stationary phase (OD_{600} >1.4) and diluting strains in fresh
547 PSY to reach an OD_{600} of ~0.8 at the time of antibiotic treatment – *e.g.* as they would be grown prior to
548 plant inoculation. Cultures were pelleted at 3250 x g for 30 minutes at RT, washed three times, then
549 resuspended in PSY to a final OD_{600} of 1.0. Four 100 µl aliquots of these culture were diluted 1:00 into
550 separate 10 mL BNM cultures in clear glass tubes in plant growth chambers. Kanamycin (at 25, 50, 75,
551 and 100 µg/mL) and streptomycin (at 25, 50, 75, and 100 µg/mL) were added directly to the BNM
552 cultures, and 100 µl samples were taken immediately prior to antibiotic treatment and at 2, 4, 6, 8, and 10
553 hours post-antibiotic addition. These 100 µl samples were immediately diluted 1:10 in 900 µl and mixed

554 vigorously by repeated pipetting. Vortexing was avoided as we found that this method reduces Δ*hpnH*
555 viability. Ten serial 1:10 dilutions were performed, and three 10 µl samples of each dilution for each strain
556 were spotted and dripped across PSY plates. After 7 days (wild type) or 10 days (Δ*hpnH*), colonies were
557 counted manually and recorded for each dilution exhibiting discrete colonies. Log plots of colony counts
558 over time were generated in R.
559 Plants were then inoculated with Δ*hpnH* and wild-type *B. diazoefficiens* as described above, and
560 kanamycin and streptomycin were added to Δ*hpnH*-inoculated plants to 50 µg/mL each, and to wild type-
561 inoculated plants to 100 µg/mL at 12 hours and 36 hours and at 2, 2.5, 3, 3.5, 4, 4.5, 5, 6.5, 8.5, 9.5, 10.5,
562 and 12.5 days post-inoculation. Four plants were treated per time point per strain, with an additional four
563 plants each as an untreated control. At 40 dpi, the number of nodules per plant was recorded.
564
565 *Bulk motility assays*
566 Swimming motility assays were performed as previously described, with some modifications
567 (Althabegoiti et al. 2008). WT and Δ*hpnH* were grown to turbidity in 5 mL of PSY at 30°C and 250 rpm,
568 diluted to an OD_{600} of 0.02 in 5 mL of fresh PSY, and grown to exponential phase (OD_{600} = 0.3-0.5).
569 Exponential cultures then were diluted to an OD_{600} of 0.06 in fresh PSY and 2 µL of the adjusted cultures
570 into the center of swimming plate containing 0.3% agar/PSY. After inoculation, the plates were wrapped
571 with parafilm to prevent dehydration and incubated in a humidity-controlled environmental chamber
572 (Percival) at 30°C for 10 days total, with daily scans after 5 days. The resulting images were analyzed in
573 FIJI to measure the area of the swimming colony.
574
575 *Surface attachment assays*
576 Δ*hpnH* and wild-type *B. diazoefficiens* were grown in 5 mL PSY cultures to stationary phase
577 (OD_{600} >1.4) then diluted in fresh PSY to reach an OD_{600} of ~0.8 at the time of surface attachment
578 assays. Cultures were pelleted at 3250 x g for 30 minutes at RT, washed twice in the indicated
579 attachment medium, then resuspended in attachment medium to an OD_{600} of 1.0. These cultures were
580 mixed thoroughly by repeated pipetting, and 2 mL samples were added to sterile imaging dishes (30 mm
581 dishes with 20 mm, #1.5 coverglass bottoms; MatTek). Cultures were incubated on imaging dishes

582 *without shaking* at 30°C for two hours. To remove non-adhered cells, imaging dishes were immersed in
583 50 mL of attachment media in a 100 mL glass beaker on an orbital shaker and shaken gently at RT for 5
584 minutes; direct application of washing medium to the coverglass surface was avoided, as we found that
585 this creates a shear force sufficient to wash away adhered cells. Imaging dishes were then gently lifted
586 out of the washing medium and imaged with a 100X objective on a Lumascope 720 fluorescence
587 microscope (Etaluma). Forty fields of view were recorded for each strain and media combination. These
588 images were processed in FIJI using the Enhanced Local Contrast (CLAHE) plugin (Heckbert and Karel
589 1994) and converted into a binary image to determine the area of the imaging window covered with
590 adhered cells. Calculation of the fraction of the surface was performed in Excel and statistical analyses
591 were conducted in R. Areas of the surface containing groups of cells larger than 10 μm^2 in area were
592 ignored in the calculations, as these likely do not represent true attachment events rather than
593 sedimentation of larger cell clumps. BNM used for attachment assays was prepared as described above,
594 with the addition of 1.0 g/mL arabinose. Because BNM contains salt crystals that can sediment onto
595 coverglass and occlude or obscure adhered cells, this medium was passed through a 2 µm filter
596 (Millipore) prior to the attachment experiments.
597
598 *Single-cell motility assays and analysis*
599 B. diazoefficiens wild-type and ΔhpnH were grown in 12.5 ml PSY medium at 30°C and 200 rpm
600 to an OD_{600} = 0.6-0.8 from an AG medium plate culture. Then, a 1:10 dilution of cell culture was
601 subcultured in PSY medium to a final volume of 12.5 ml and regrown to an OD_{600} of ~0.6. Two aliquots of
602 750 µL were sampled from the regrowth culture and pelleted at 3500 x g for 20 min (wild-type) or for 30
603 min (ΔhpnH) at RT. The supernatant was removed, and one pellet was resuspended in 500 µL PSY and
604 the other in 500 µL BNM medium. Because BNM contains salt crystals that can sediment onto coverglass
605 and occlude or obscure adhered cells, this medium was passed through a 2 µm filter (Millipore) prior to
606 usage for these experiments. The two medium conditions were then incubated for 2.5 hrs (wild-type) or
607 for 3.5 hrs (ΔhpnH) at 30°C; given the difference in growth time ΔhpnH incubated for longer. Right before
608 imaging, each culture was diluted at a 1:10 ratio with its respective medium. The bacteria were then

injected into a sterile flow cell (ibidi sticky-Slide VI0.4 with a glass coverslip). The flow cell was attached to a heating stage set to 30°C.

The imaging protocol involved high-speed bright-field imaging for 5 min at a single XYZ location per experimental repeat. High speed bright-field recordings used a Phantom V12.1 high speed camera (Vision Research); images were taken with a 5 ms exposure at 200 fps and a resolution of 512×512 pixels (0.1 μm/pixel). This protocol was performed on an Olympus IX83 microscope equipped with a 100× oil objective, a 2× multiplier lens, and a Zero Drift Correction autofocus system. The recorded movies were extracted into single frames from the .cine files using PCC 2.8 (Phantom Software). Image processing and cell tracking algorithms are adapted from previous work (Lee et al. 2018) and written in MATLAB R2015a (Mathworks).

We identified cells swimming near the surface as cells with a trajectory radius of gyration greater than 2.5 μm and a mean-squared displacement (MSD) slope greater than 1.5. Setting a minimum radius of gyration selects for cells with a minimum net translation on the across the surface, while a minimum MSD slope threshold ensured the cells are moving super-diffusively (MSD slope ≅ 1, diffusive motion; MSD slope ≅ 2, super-diffusive motion). For each tracked cell, the mean-speed, **v**, was calculated by averaging a moving window, **w**, of the displacement over the cell's full trajectory, using the following equation:

$$< v > = \; Avg\left(\sum_{\square=1}^{N-w} \frac{\sqrt{(x_{t+w} - x_t)^2 + (y_{t+w} - y_t)^2}}{w} * f * p\right)$$

where **N** is the total number of points in the trajectory, **f** is the acquisition frame rate, and **p** is the pixel resolution. Here we set a window size, w= 40 frames. All analysis and visualizations from these experiments where done using MATLAB R2015a (Mathworks).

Acknowledgements

This work was supported by grants from the HHMI (D.K.N.), NASA (NNX12AD93G, D.K.N.), Jane Coffin Childs Memorial Fund (B.J.B.), NIH (K99GM126141,

635 B.J.B.), and Army Research Office (W911NF-18-1-0254, GW) and predoctoral fellowships from NSF
636 (E.T.) and the Ford Foundation (J.d.A.). We thank Dr. Eric Giraud for his generous gift of *A. afraspera*
637 seeds and training on *Aeschynomene* symbioses and Drs. Hans-Martin Fischer and Raphael Ledermann
638 for plasmids and technical advice for the genetic transformation of *B. diazoefficiens*. Dr. Nathan Dalleska
639 of the Environmental Analysis Center at Caltech was instrumental in providing training and support for
640 GC-MS analysis of acetylene reduction. We are grateful to Dr. Gargi Kulkarni and other members of the
641 Newman lab, as well as Drs. Elliot Meyerowitz and Rob Phillips, for their collegiality and thoughtful
642 discussions about this work. We are indebted to Ms. Shannon Park and Ms. Kristy Nguyen for providing
643 the administrative assistance that allows us to focus on our research.
644

645 **References**

646 Abeysekera, R. M., Newcomb, W., Silvester, W. B., and Torrey, J. G. 1990. A freeze-fracture electron
647 microscopic study of *Frankia* in root nodules of *Alnus incana* grown at three oxygen tensions. Can.
648 J. Microbiol. 36:97–108
649 Barriere, Q., Guefrachi, I., Gully, D., Lamouche, F., Pierre, O., Fardoux, J., Chaintreuil, C., Alunni, B.,
650 Timchenko, T., Giraud, E., and Mergaert, P. 2017. Integrated roles of BclA and DD-
651 carboxypeptidase 1 in *Bradyrhizobium* differentiation within NCR-producing and NCR-lacking root
652 nodules. Sci. Rep. 7:9063
653 Belin, B. J., Busset, N., Giraud, E., Molinaro, A., Silipo, A., and Newman, D. K. 2018. Hopanoid lipids:
654 from membranes to plant-bacteria interactions. Nat. Rev. Microbiol. 16:304–315
655 Bonaldi, K., Gargani, D., Prin, Y., Fardoux, J., Gully, D., Nouwen, N., Goormachtig, S., and Giraud, E.
656 2011. Nodulation of *Aeschynomene afraspera* and *A. indica* by photosynthetic *Bradyrhizobium* Sp.
657 strain ORS285: the nod-dependent versus the nod-independent symbiotic interaction. Mol. Plant.
658 Microbe. Interact. 24:1359–1371
659 Bradley, A. S., Swanson, P. K., Muller, E. E. L., Bringel, F., Caroll, S. M., Pearson, A., Vuilleumier, S., and
660 Marx, C. J. 2017. Hopanoid-free *Methylobacterium extorquens* DM4 overproduces carotenoids and
661 has widespread growth impairment. PLoS One. 12:e0173323
662 Caamal-Fuentes, E., Peraza-Sánchez, S., Torres-Tapia, L., and Moo-Puc, R. 2015. Isolation and

663 identification of cytotoxic compounds from *Aeschynomene fascicularis*, a Mayan medicinal plant.
664 Molecules. 20:13563–13574
665 Chifundera, K. 2001. Contribution to the inventory of medicinal plants from the Bushi area, South Kivu
666 Province, Democratic Republic of Congo. Fitoterapia. 72:351–368
667 Czernic, P., Gully, D., Cartieaux, F., Moulin, L., Guefrachi, I., Patrel, D., Pierre, O., Fardoux, J.,
668 Chaintreuil, C., Nguyen, P., Gressent, F., Da Silva, C., Poulain, J., Wincker, P., Rofidal, V., Hem, S.,
669 Barrière, Q., Arrighi, J.-F., Mergaert, P., and Giraud, E. 2015. Convergent evolution of endosymbiont
670 differentiation in Dalbergioid and Inverted Repeat-Lacking Clade legumes mediated by nodule-
671 specific cysteine-rich peptides. Plant Physiol. 169:1254–1265
672 Ehrhardt, D. W., Atkinson, E. M., and Long, S. R. 1992. Depolarization of alfalfa root hair membrane
673 potential by *Rhizobium meliloti* Nod factors. Science. 256:998–1000
674 Gupta, R., Sharma, M., and Mittal, A. 2006. Effects of membrane tension on nanopropeller driven
675 bacterial motion. J Nanosci Nanotechnol. 6:3854–3862
676 Hammad, Y., Nalin, R., Marechal, J., Fiasson, K., Pepin, R., Berry, A. M., Normand, P., and Domenach,
677 A.-M. 2003. A possible role for phenyl acetic acid (PAA) on *Alnus glutinosa* nodulation by *Frankia*.
678 Plant Soil. 254:193–205
679 Heckbert, P. S., and Karel. 1994. *Graphics gems IV*. AP Professional.
680 Keymer, A. 2018. Cross-kingdom lipid transfer in arbuscular mycorrhiza symbiosis and beyond. Curr.
681 Opin. Plant Biol. 44:137–144
682 Komaniecka, I., Choma, A., Mazur, A., Duda, K. A., Lindner, B., Schwudke, D., and Holst, O. 2014.
683 Occurrence of an unusual hopanoid-containing lipid A among lipopolysaccharides from
684 *Bradyrhizobium* species. J. Biol. Chem. 289:35644–35655
685 Kulkarni, G., Busset, N., Molinaro, A., Gargani, D., Chaintreuil, C., Silipo, A., Giraud, E., and Newman, D.
686 K. 2015. Specific hopanoid classes differentially affect free-living and symbiotic states of
687 *Bradyrhizobium diazoefficiens*. MBio. 6:e01251-15
688 Ledermann, R., Bartsch, I., Muller, B., Wulser, J., and Fischer, H.-M. 2018. A functional general stress
689 response of *Bradyrhizobium diazoefficiens* is required for early stages of host plant infection. Mol.
690 Plant. Microbe. Interact. 31:537–547

691 Ledermann, R., Bartsch, I., Remus-Emsermann, M. N., Vorholt, J. A., and Fischer, H.-M. 2015. Stable
692 fluorescent and enzymatic tagging of *Bradyrhizobium diazoefficiens* to analyze host-plant infection
693 and colonization. Mol. Plant. Microbe. Interact. 28:959–967
694 Lee, C. K., de Anda, J., Baker, A. E., Bennett, R. R., Luo, Y., Lee, E. Y., Keefe, J. A., Helali, J. S., Ma, J.,
695 Zhao, K., Golestanian, R., O'Toole, G. A., and Wong, G. C. L. 2018. Multigenerational memory and
696 adaptive adhesion in early bacterial biofilm communities. Proc. Natl. Acad. Sci. U. S. A. 115:4471–
697 4476
698 Lei, Z.-Y., Chen, J.-J., Cao, Z.-J., Ao, M.-Z., and Yu, L.-J. 2018. Efficacy of *Aeschynomene indica* Linn
699 leaves for wound healing and isolation of active constituent. J. Ethnopharmacol. 228:156-163
700 Neubauer, C., Dalleska, N. F., Cowley, E. S., Shikuma, N. J., Wu, C.-H., Sessions, A. L., and Newman,
701 D. K. 2015. Lipid remodeling in *Rhodopseudomonas palustris* TIE-1 upon loss of hopanoids and
702 hopanoid methylation. Geobiology. 13:443–453
703 Ochs, D., Kaletta, C., Entian, K., Beck-sickinger, A., Porallal, K., Chemie, O., Tubingen, U., and Institut, B.
704 1992. Cloning, expression, and sequencing of squalene-hopene cyclase,. 174:298–302
705 Parsons, R., Silvester, W. B., Harris, S., Gruijters, W. T., and Bullivant, S. 1987. *Frankia* vesicles provide
706 inducible and absolute oxygen protection for nitrogenase. Plant Physiol. 83:728–731
707 Persat, A. 2017. Bacterial mechanotransduction. Curr. Opin. Microbiol. 36:1–6
708 Petrova, O. E., and Sauer, K. 2012. Sticky situations: Key components that control bacterial surface
709 attachment. J. Bacteriol. 194:2413–2425
710 Pini, F., East, A. K., Appia-Ayme, C., Tomek, J., Karunakaran, R., Mendoza-Suarez, M., Edwards, A.,
711 Terpolilli, J. J., Roworth, J., Downie, J. A., and Poole, P. S. 2017. Bacterial biosensors for *in vivo*
712 spatiotemporal mapping of root secretion. Plant Physiol. 174:1289–1306
713 Regensburger, B., and Hennecke, H. 1983. RNA polymerase from *Rhizobium japonicum*. Arch. Microbiol.
714 135:103–109
715 Ricci, J. N., Coleman, M. L., Welander, P. V., Sessions, A. L., Summons, R. E., Spear, J. R., and
716 Newman, D. K. 2014. Diverse capacity for 2-methylhopanoid production correlates with a specific
717 ecological niche. ISME J. 8:675–684
718 Richards, F. J. 1959. NA Flexible growth function for empirical use. J. Exp. Bot. 10:290–301

719 Saenz, J. P., Grosser, D., Bradley, A. S., Lagny, T. J., Lavrynenko, O., Broda, M., and Simons, K. 2015.
720 Hopanoids as functional analogues of cholesterol in bacterial membranes. Proc. Natl. Acad. Sci. U.
721 S. A. 112:11971–11976
722 Schindelin, J., Arganda-Carreras, I., Frise, E., Kaynig, V., Longair, M., Pietzsch, T., Preibisch, S.,
723 Rueden, C., Saalfeld, S., Schmid, B., Tinevez, J. Y., White, D. J., Hartenstein, V., Eliceiri, K.,
724 Tomancak, P., and Cardona, A. 2012. Fiji: An open-source platform for biological-image analysis.
725 Nat. Methods. 9:676–682
726 Schmerk, C. L., Welander, P. V, Hamad, M. A., Bain, K. L., Bernards, M. A., Summons, R. E., and
727 Valvano, M. A. 2015. Elucidation of the *Burkholderia cenocepacia* hopanoid biosynthesis pathway
728 uncovers functions for conserved proteins in hopanoid-producing bacteria. Environ. Microbiol.
729 17:735–750
730 Schneider, C. A., Rasband, W. S., and Eliceiri, K. W. 2012. NIH Image to ImageJ: 25 years of image
731 analysis. Nat. Methods. 9: 671-675
732 Silipo, A., Vitiello, G., Gully, D., Sturiale, L., Chaintreuil, C., Fardoux, J., Gargani, D., Lee, H.-I., Kulkarni,
733 G., Busset, N., Marchetti, R., Palmigiano, A., Moll, H., Engel, R., Lanzetta, R., Paduano, L., Parrilli,
734 M., Chang, W.-S., Holst, O., Newman, D. K., Garozzo, D., D'Errico, G., Giraud, E., and Molinaro, A.
735 2014. Covalently linked hopanoid-lipid A improves outer-membrane resistance of a *Bradyrhizobium*
736 symbiont of legumes. Nat. Commun. 5:5106
737 Somado, E. A., Becker, M., Kuehne, R. F., Sahrawat, K. L., and Vlek, P. L. G. 2003. Combined effects of
738 legumes with rock phosphorus on rice in West Africa. Agron. J. 95:1172
739 Sugiyama, A., and Yazaki, K. 2012. Root exudates of legume plants and their involvement in interactions
740 with soil microbes. In: Vivanco J., Baluška F. (eds) Secretions and exudates in biological systems.
741 signaling and communication in plants, vol 12. Springer, Berlin, Heidelberg
742 Swapna M.M, S., R., P., K.P., A., C.N, M., and N.P, R. 2011. A review on the medicinal and edible
743 aspects of aquatic and wetland plants of India. J. Med. Plants Res. 5:7163–7176
744 Syren, P.-O., Henche, S., Eichler, A., Nestl, B. M., and Hauer, B. 2016. Squalene-hopene cyclases-
745 evolution, dynamics and catalytic scope. Curr. Opin. Struct. Biol. 41:73–82
746 Szparaga, A., and Kocira, S. 2018. Generalized logistic functions in modelling emergence of *Brassica*

747 *napus* L. PLoS One. 13:1–14
748 Vilcheze, C., Llopiz, P., Neunlist, S., Poralla, K., and Rohmer, M. 1994. Prokaryotic triterpenoids: New
749 hopanoids from the nitrogen-fixing bacteria *Azotobacter vinelandii*, *Beijerinckia indica* and
750 *Beijerinckia mobilis*. Microbiology. 140:2749–2753
751 Welander, P. V, Coleman, M. L., Sessions, A. L., Summons, R. E., and Newman, D. K. 2010.
752 Identification of a methylase required for 2-methylhopanoid production and implications for the
753 interpretation of sedimentary hopanes. Proc. Natl. Acad. Sci. U. S. A. 107:8537–8542
754 Welander, P. V, Doughty, D. M., Wu, C., Mehay, S., and Roger, E. 2012. Identification and
755 characterization of *Rhodopseudomonas palustris* TIE-1 hopanoid biosynthesis mutants. 10:163–177
756 Wheatley, R. M., and Poole, P. S. 2018. Mechanisms of bacterial attachment to roots. FEMS Microbiol.
757 Rev. 42:448–461
758 Wu, C.-H., Bialecka-Fornal, M., and Newman, D. K. 2015. Methylation at the C-2 position of hopanoids
759 increases rigidity in native bacterial membranes. Elife. 4
760
761 **Figure Legends**
762
763 **Figure 1. The nitrogen fixation defect of Δ*hpnH* results from a reduction in nodule sizes.** (**a**)
764 Chemical structure of the extended hopanoid 2-Methyl Bacteriohopanetetrol (2Me-BHT), consisting of a
765 central pentacyclic core synthesized by the *shc* gene product, a C2 methylation site added by the product
766 of *hpnP* (grey shading, left), and a tetrol group added by the *hpnH* product (grey shading, right). (**b**)
767 Average shoot heights and nodules per plant at 24 dpi for *A. afraspera* plants inoculated with wild-type,
768 Δ*hpnH* or Δ*hpnP B. diazoefficiens.* (**c**) Average acetylene reduction per plant and per nodule at 24 dpi for
769 *A. asfrapera* plants inoculated with wild-type, Δ*hpnH* or Δ*hpnP*. (**d**) Representative confocal images of
770 cross-sections of wild type- and Δ*hpnH*-infected nodules at 24 dpi illustrating plant cell walls (Calcofluor,
771 cyan), live bacteria (SYTO9, yellow) and membrane-compromised bacteria and plant nuclei (propidium
772 iodide, magenta). (**e**) Average nodule dry mass and acetylene reduction per nodule dry mass at 24 dpi for
773 plants inoculated with wild-type, Δ*hpnH* or Δ*hpnP*. Data shown in (**b**), (**c**) and (**e**) was collected from n = 8

774 plants, with error bars representing one standard deviation. Results of two-tailed t-tests between wild type
775 and Δ*hpnH* or Δ*hpnP* are denoted as follows: n.s., p>0.01; *, p<0.01; **, p<0.001; ***, p<0.0001.
776
777 **Figure 2. Smaller Δ*hpnH* nodules are offset by increased nodule size heterogeneity over time.** (**a**)
778 Average acetylene reduction per plant (n=4 plants per bar) and (**b**) average nodule dry mass per plant
779 (n=8 plants per bar) for *A. asfrapera* inoculated with wild-type or Δ*hpnH* over time. Error bars representing
780 one standard deviation. Results of two-tailed t-tests between wild type and Δ*hpnH* are denoted as follows:
781 n.s., p>0.05; *, p<0.05; ***, p<0.0001. (**c-d**) *A. afraspera* inoculated with wild type or Δ*hpnH* at (**c**) 20 dpi
782 (left) and at (**d**) 40 dpi (right). (**e-f**) Distributions of nodule diameters at 40 dpi for *A. afraspera* inoculated
783 with (**e**) Δ*hpnH* (right; n=268 nodules pooled from 10 plants) or (**f**) wild type (left; n=227 nodules pooled
784 from 10 plants).
785
786 **Figure 3. Nodules containing Δ*hpnH* emerge later and have more heterogeneous growth rates and**
787 **final volumes than wild type.** (**a**) Comparison of the development of selected wild type- and Δ*hpnH*-
788 infected nodules over time. (**b**) Nodule growth plots for 74 wild type-infected nodules tracked from 10
789 plants. (**c**) Nodule growth plots for 84 Δ*hpnH*-infected nodules tracked from 16 plants. (**d**) Schematic of
790 nodule development in *A. afraspera*. From the left, bacteria (in blue) colonize and invade plant roots
791 (green) and intracellularly infect a root cell (pink); the time of this initial intracellular infection is considered
792 $\mathbf{t_i}$ and the nodule volume can be described as the volume of the single infected root cell, $\mathbf{V_i}$. This infected
793 cell proliferates to form a spherical nodule that is visible to the naked eye, at time $\mathbf{t_{min}}$ and volume $\mathbf{V_{min}}$.
794 The infected plant cells continue to proliferate at rate **dV/dt** until the nodule has fully matured at time $\mathbf{t_{max}}$
795 and volume $\mathbf{V_{max}}$. (**e**) Fitted growth curve for a sample wild-type nodule illustrating the positions of $\mathbf{t_{min}}$,
796 $\mathbf{V_{min}}$, **dV/dt**, $\mathbf{t_{max}}$, and $\mathbf{V_{max}}$. (**f-g**) Jitter and box plots of (**f**) **dV/dt** and (**g**) $\mathbf{V_{max}}$ values for all wild type- and
797 Δ*hpnH*-infected nodules. Results of KS-tests between wild-type and Δ*hpnH* nodules are denoted as
798 follows: ***, $p<10^{-6}$. (**h**) Scatter plots of **dV/dt** vs. $\mathbf{V_{max}}$ values for wild-type and Δ*hpnH* nodules. Values of
799 **dV/dt** and $\mathbf{V_{max}}$ below what is observed in the wild-type dataset are highlighted in green. (**i**) Distributions
800 of $\mathbf{t_{min}}$ values (as observed by eye) for nodules from wild type- (white bars) or Δ*hpnH*- (grey bars) infected
801 plants. N=457 wild-type nodules across 20 plants and 479 Δ*hpnH* nodules across 20 plants.

802

803 **Figure 4. Small Δ*hpnH* nodules are under-infected compared to wild type.** (**a**) Confocal sections of
804 small (<0.5 mm radius) Δ*hpnH*-infected nodules harvested at 40 dpi and small (<0.5 mm radius) wild
805 type-infected nodules harvested at 10 and 25 dpi. (**b**) Confocal sections of larger (>0.5 mm radius)
806 Δ*hpnH*- or wild type-infected nodules harvested at 40 dpi.

807

808 **Figure 5. Extended hopanoid mutants are delayed at pre-intracellular stage(s) in symbiosis**
809 **development.** (**a**) Confocal sections of nodules from plants co-inoculated with wild type-YFP and Δ*hpnH*-
810 mCherry harvested at 45-55 dpi. Sections were stained with Calcofluor (cyan) and are expressing YFP
811 (yellow) and mCherry (magenta). (**b**) Scatter plot of median YFP intensity per pixel normalized by
812 propidium iodide intensity per pixel (*e.g.* bacteroid density) within infection zones of nodules from plants
813 co-inoculated with wild type-YFP and wild type, as a function of the percentage of wild type-YFP in the
814 inoculum. (**c**) Scatter plot of median propidium iodide intensity per pixel (*e.g.* bacteroid density) within
815 infection zones of nodules from plants co-inoculated with YFP-tagged wild type and untagged wild type,
816 as a function of the percentage of WT-YFP in the inoculum. (**d**) Colony forming units/mL in wild type and
817 Δ*hpnH* cultures grown in BNM supplemented with varying concentrations of kanamycin and
818 spectinomycin at various times post-inoculation. (**e**) Average nodules per plant at 40 dpi for plants
819 inoculated with either wild type or Δ*hpnH* and treated with 50 μg/mL (Δ*hpnH*) or 100 μg/mL (wild type)
820 kanamycin and streptomycin at various time points post-inoculation. Nodule counts are normalized to
821 those observed in non-antibiotic treated plants. (**f**) Images of inoculated plants at 40 dpi after antibiotic
822 treatment at various time points. Untreated plants are shown on the left, with increasing time of antibiotic
823 addition. Error bars represent one standard deviation.

824

825 **Figure 6. Extended hopanoid mutants are less motile than wild type and attach poorly to surfaces**
826 ***in vitro*.** (**a**) Sample time course of wild type and Δ*hpnH* colony expansion on low-agar PSY plates (dpi =
827 days post-inoculation). Scale bars represent 2 cm. (**b**) Average colony sizes of wild type and Δ*hpnH* over
828 time. N=4 plates per strain; error bars indicate one standard deviation. (**c**) Trajectories of individual wild
829 type (top) and Δ*hpnH* (bottom) cells over a 5 minute time course in PSY. (**d**) Distributions of mean-speed

830 s for motile wild type (N=359) and Δ*hpnH* (N=91) cells for trajectories in **d**. Dotted lines indicate the
831 means of the distributions. (**e**) Trajectories of individual wild type (top) and Δ*hpnH* (bottom) cells over a 5
832 minute time course in BNM. (**f**) Distributions of mean-speeds for motile WT (N=421) and Δ*hpnH* (N=141)
833 cells in BNM for trajectories in **e**. Dotted lines indicate the means of the distributions. (g) Jitter and box
834 plots of surface attachment (*e.g.* the percent of the field of view covered with cells) of WT and Δ*hpnH*
835 after 2 hours of incubation on glass in PSY or BNM. N=40 fields of view per condition. Results of two-
836 tailed t-tests between wild type and Δ*hpnH* are denoted as follows: n.s., $p>0.05$; ***, $p<0.00001$.
837
838 **Figure 7. Consequences of extended hopanoid loss in *A. afraspera* nodule development.**
839 Schematic representation of *A. afraspera* wild-type root nodule development (top row; white background)
840 and defects in development associated with extended hopanoid loss (bottom row; grey background).
841 Early in development, fewer Δ*hpnH* cells are motile (**a**) and competent to attach to root surfaces (**b**),
842 leading to a delay in establishment of stable root colonies. At later stages, slow growth of Δ*hpnH* into the
843 root interior, or poor uptake by and division within host cells (**c**) may generate "patchy", or under-
844 populated infection zone that is propagated as the nodule grows (**d**). Alternately, fully-infected Δ*hpnH*
845 nodules may lose symbionts to symbiont cell death (**e**) via poor bacteroid survival or plant-directed
846 symbiosome degradation.
847
848 **Supplemental Data**
849
850 **Table S1**. Motile cell counts and mean swimming speeds for wild-type and Δ*hpnH B. diazoefficiens*.

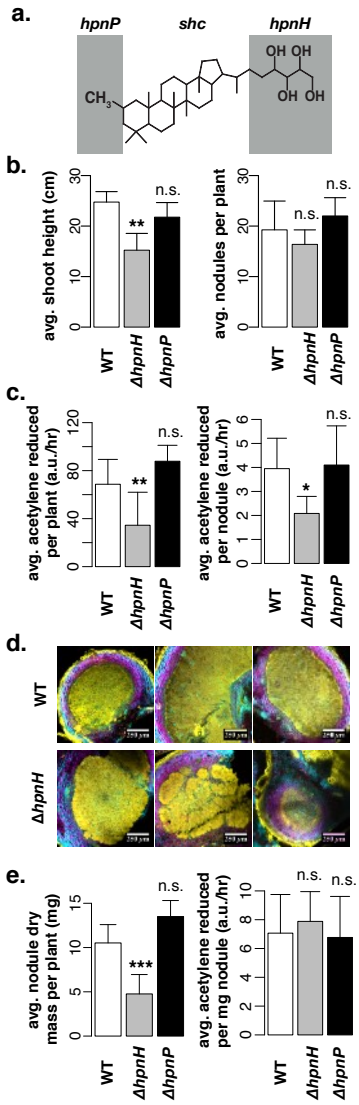
a.
hpnP
shc
hpnH
CH3
OH OH
OH OH
b.
avg. shoot height (cm)
avg. nodules per plant
n.s.
**
n.s.
WT
ΔhpnH
ΔhpnP
c.
avg. acetylene reduced per plant (a.u./hr)
avg. acetylene reduced per nodule (a.u./hr)
**
*
n.s.
d.
WT
ΔhpnH
e.
avg. nodule dry mass per plant (mg)
avg. acetylene reduced per mg nodule (a.u./hr)
***
n.s.

Figure 1.

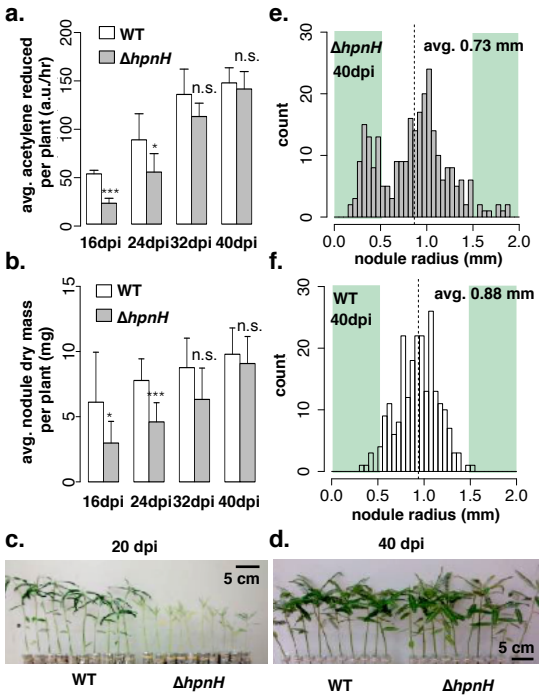
a.
WT
ΔhpnH
avg. acetylene reduced per plant (a.u./hr)
0
50
100
150
200
***
*
n.s.
n.s.
16dpi
24dpi
32dpi
40dpi
b.
WT
ΔhpnH
avg. nodule dry mass per plant (mg)
0
5
10
15
*
***
n.s.
n.s.
16dpi
24dpi
32dpi
40dpi
c.
20 dpi
5 cm
WT
ΔhpnH
d.
40 dpi
5 cm
WT
ΔhpnH
e.
ΔhpnH
40dpi
avg. 0.73 mm
count
0
10
20
30
0.0
0.5
1.0
1.5
2.0
nodule radius (mm)
f.
WT
40dpi
avg. 0.88 mm
count
0
10
20
30
0.0
0.5
1.0
1.5
2.0
nodule radius (mm)

Figure 2.

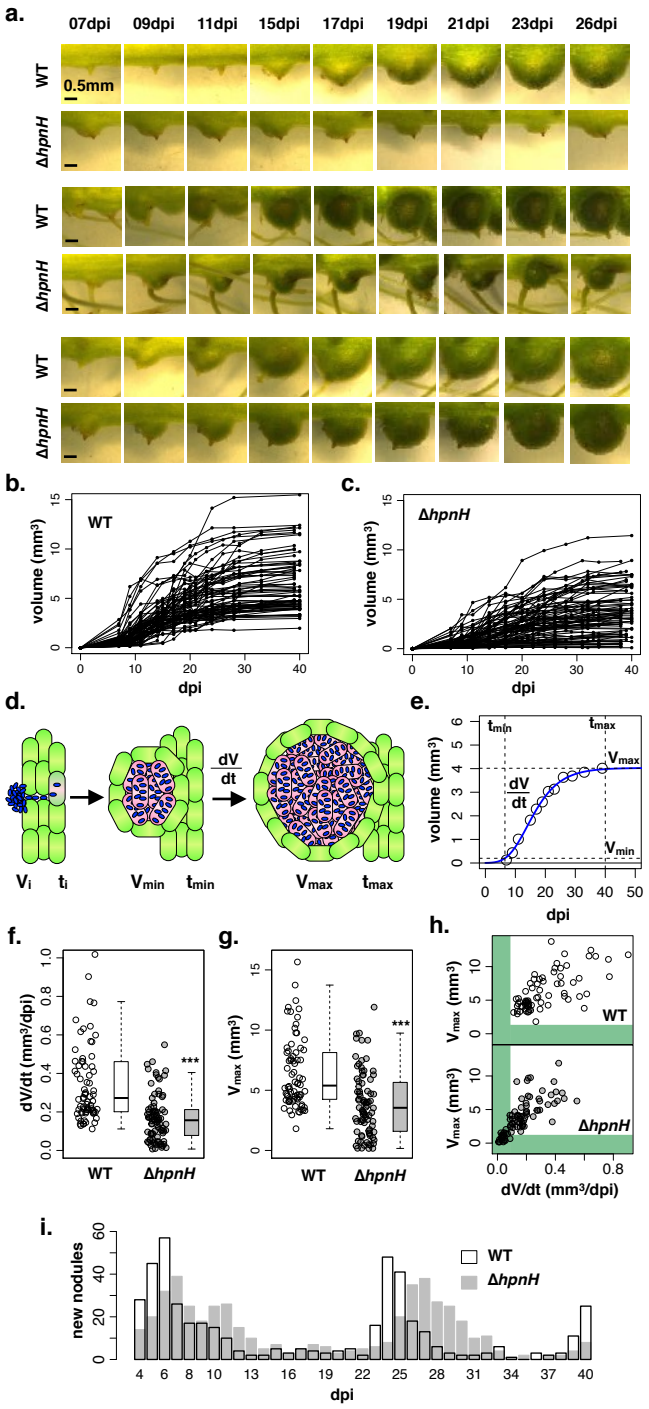
a.
07dpi
09dpi
11dpi
15dpi
17dpi
19dpi
21dpi
23dpi
26dpi
WT
ΔhpnH
0.5mm
b.
WT
volume (mm³)
dpi
c.
ΔhpnH
volume (mm³)
dpi
d.
dV
dt
Vi
ti
Vmin
tmin
Vmax
tmax
e.
tmin
tmax
Vmax
Vmin
dV
dt
volume (mm³)
dpi
f.
dV/dt (mm³/dpi)
***
WT
ΔhpnH
g.
Vmax (mm³)
***
WT
ΔhpnH
h.
Vmax (mm³)
WT
ΔhpnH
dV/dt (mm³/dpi)
i.
new nodules
WT
ΔhpnH
dpi

Figure 3.

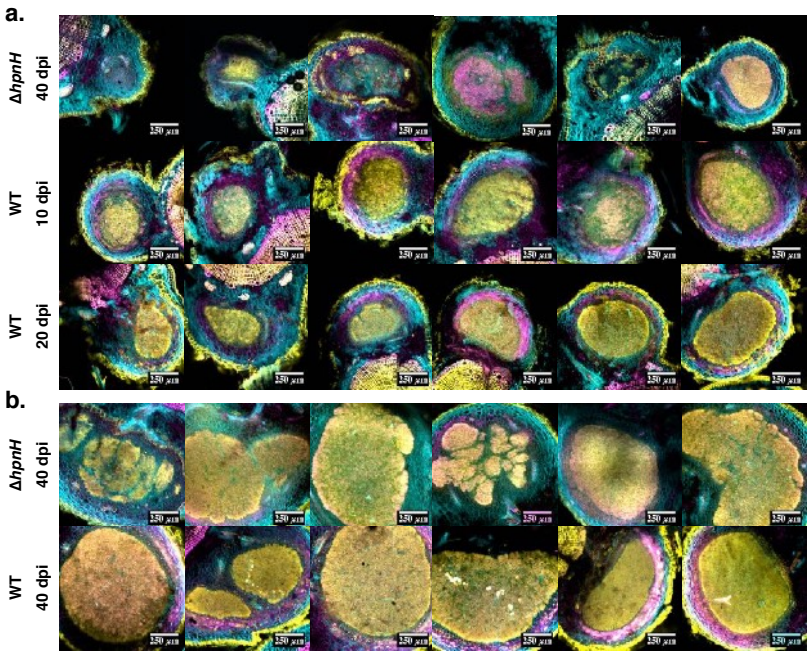

Figure 4.

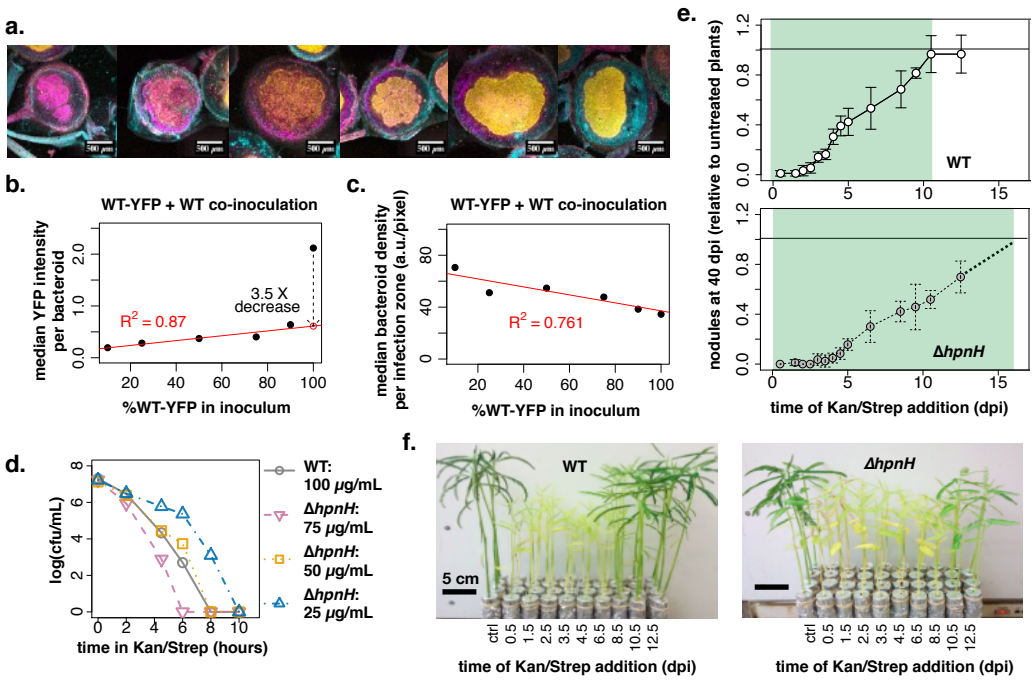
a.
b.
WT-YFP + WT co-inoculation
median YFP intensity per bacteroid
3.5 X decrease
R^2 = 0.87
%WT-YFP in inoculum
c.
WT-YFP + WT co-inoculation
median bacteroid density per infection zone (a.u./pixel)
R^2 = 0.761
%WT-YFP in inoculum
e.
nodules at 40 dpi (relative to untreated plants)
WT
ΔhpnH
time of Kan/Strep addition (dpi)
d.
log(cfu/mL)
time in Kan/Strep (hours)
WT: 100 μg/mL
ΔhpnH: 75 μg/mL
ΔhpnH: 50 μg/mL
ΔhpnH: 25 μg/mL
f.
WT
ΔhpnH
5 cm
ctrl 0.5 1.5 2.5 3.5 4.5 6.5 8.5 10.5 12.5
time of Kan/Strep addition (dpi)

Figure 5.

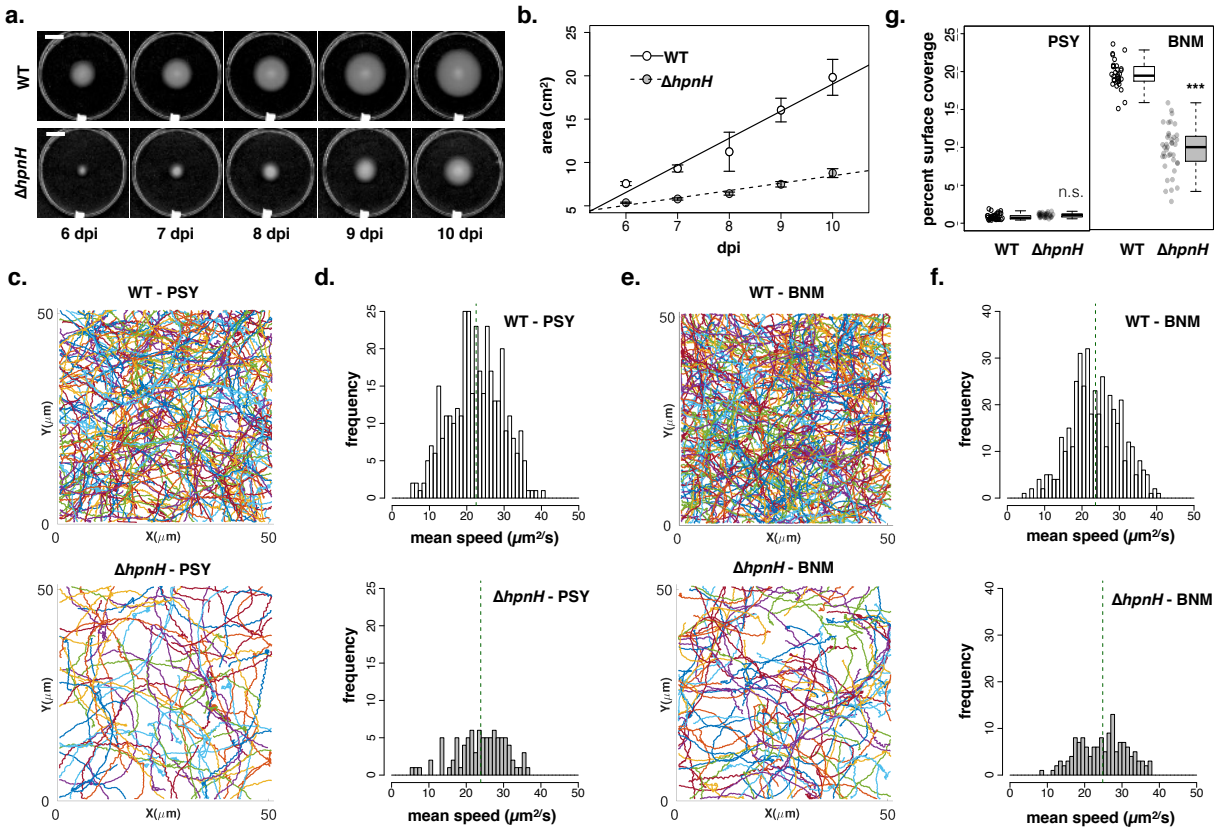
a.
WT
ΔhpnH
6 dpi
7 dpi
8 dpi
9 dpi
10 dpi
b.
WT
ΔhpnH
area (cm²)
dpi
g.
PSY
BNM
percent surface coverage
n.s.
***
WT
ΔhpnH
WT
ΔhpnH
c.
WT - PSY
ΔhpnH - PSY
Y(μm)
X(μm)
d.
WT - PSY
ΔhpnH - PSY
frequency
mean speed (μm²/s)
e.
WT - BNM
ΔhpnH - BNM
Y(μm)
X(μm)
f.
WT - BNM
ΔhpnH - BNM
frequency
mean speed (μm²/s)

Figure 6.

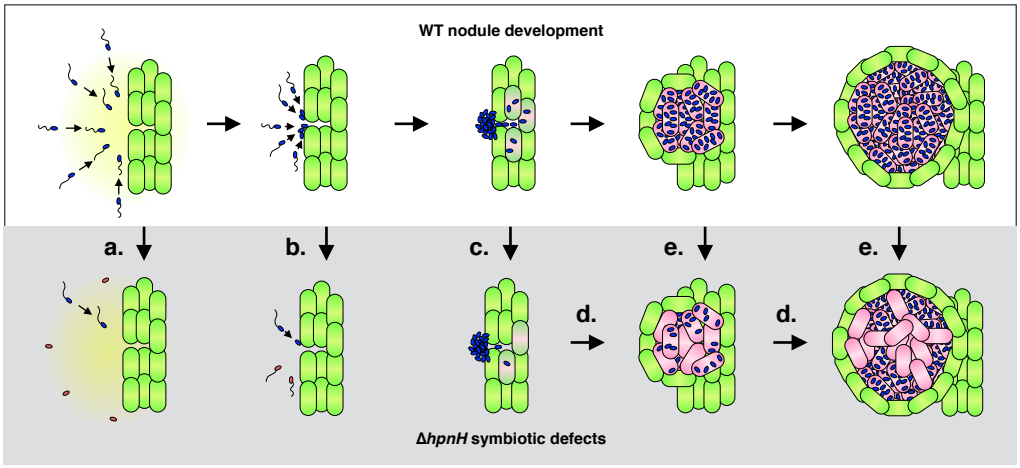

Figure 7.

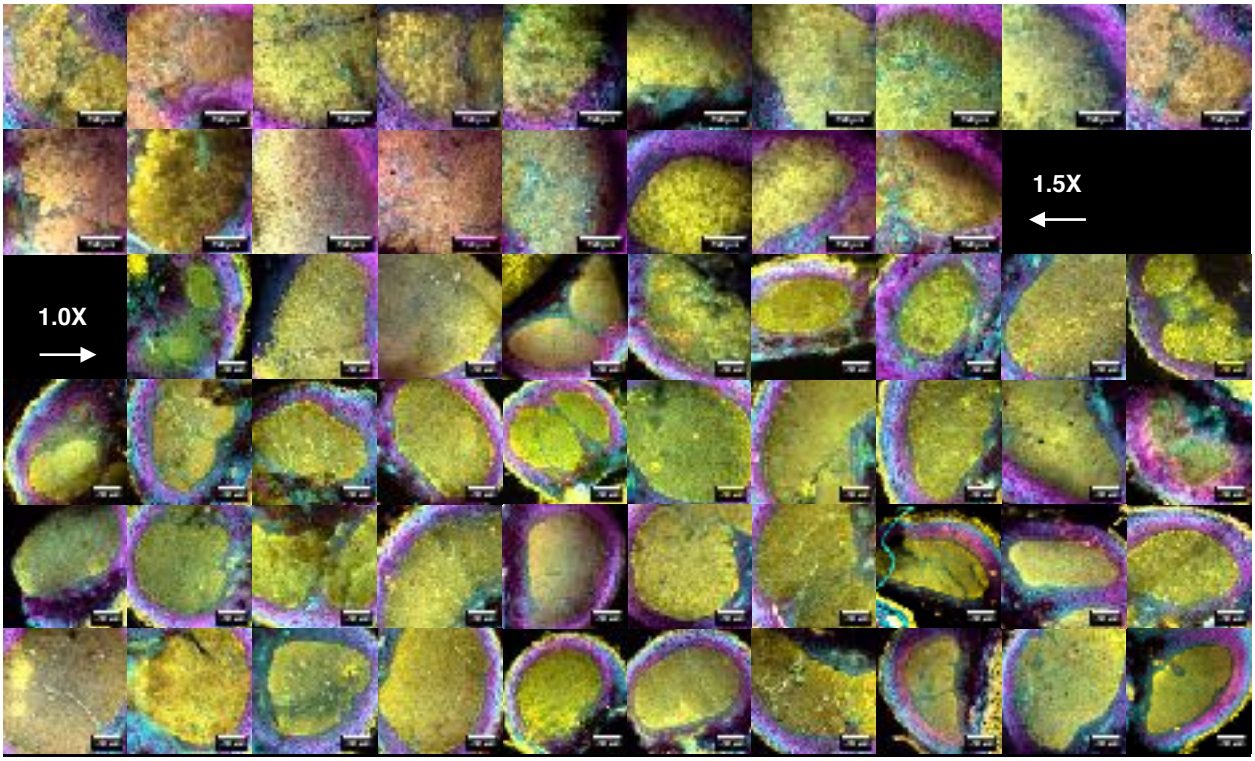

Figure S1. Confocal images of cross-sections of wild type-infected *A. afraspera* nodules at 24 dpi illustrating plant cell walls (Calcofluor, cyan), live bacteria (SYTO9, yellow) and membrane-compromised bacteria and plant nuclei (propidium iodide, magenta). Nodules were collected from 3 plants.

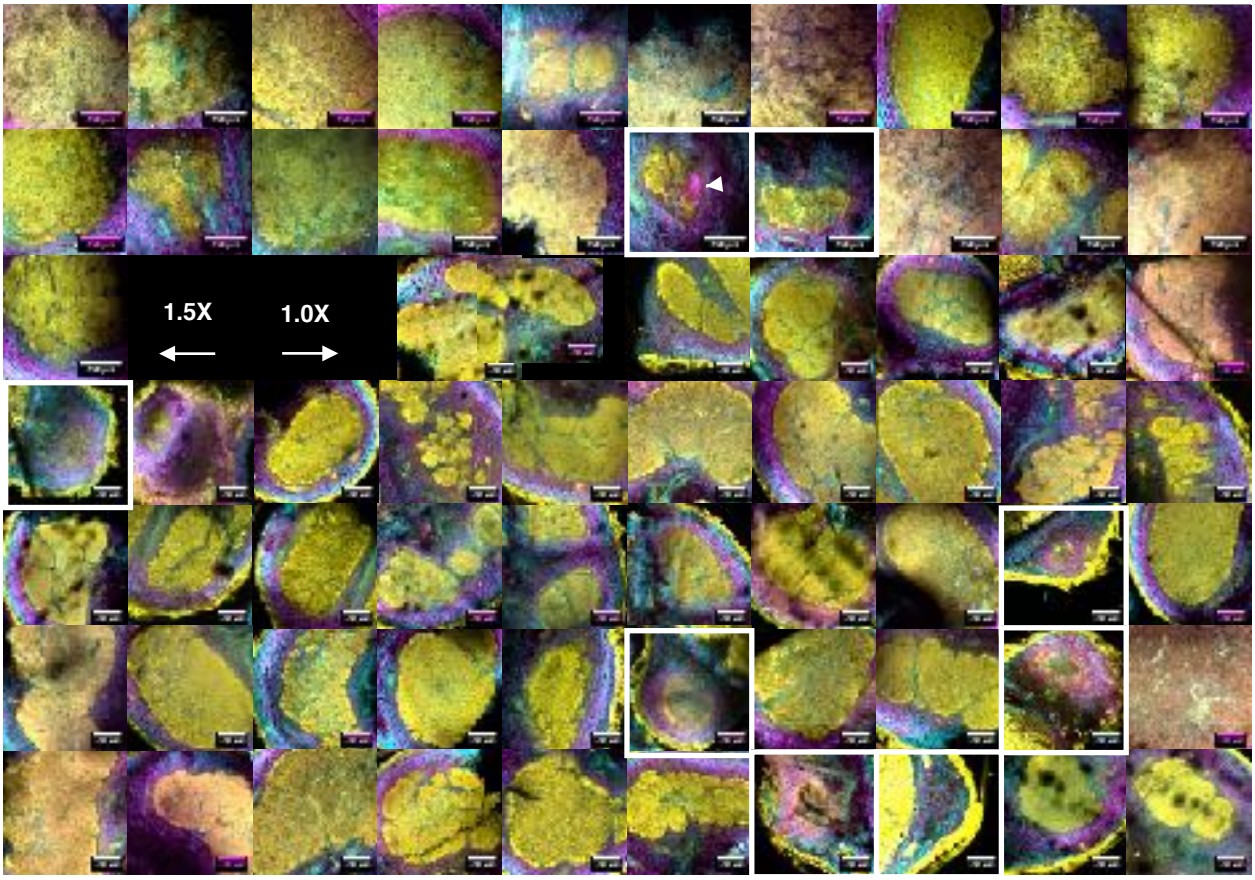

Figure S2. Confocal images of cross-sections of Δ*hpnH*-infected *A. afraspera* nodules at 24 dpi illustrating plant cell walls (Calcofluor, cyan), live bacteria (SYTO9, yellow) and dead bacteria and plant nuclei (propidium iodide, magenta). Nodules were collected from 3 plants. White boxes highlight small nodules. White arrow indicates a likely plant defense reaction.

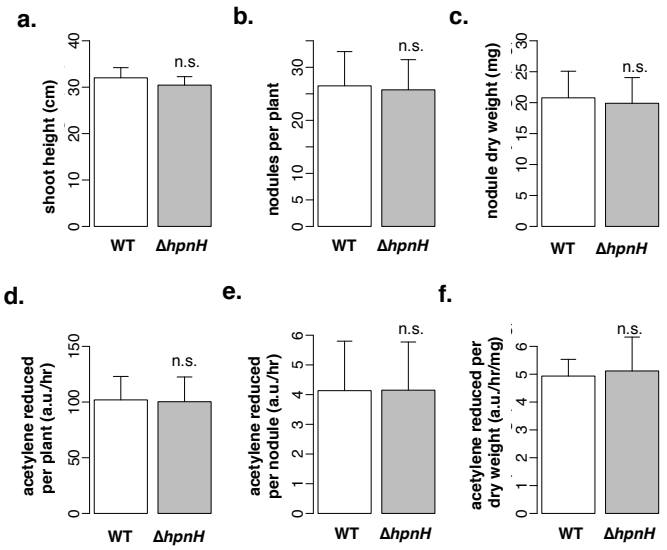

Figure S3. Average (**a**) shoot height, (**b**) nodules per plant, (**c**) nodule dry weight per plant, (**d**) acetylene reduction per plant, (**e**) acetylene reduction per nodule, and (**f**) acetylene reduction per nodule dry weight for *A. asfrapera* inoculated with wild-type or Δ*hpnH* at 40 dpi. N=4 plants per bar; error bars represent one standard deviation. Results of two-tailed t-tests between wild type and Δ*hpnH* are denoted as follows: n.s., p>0.05.

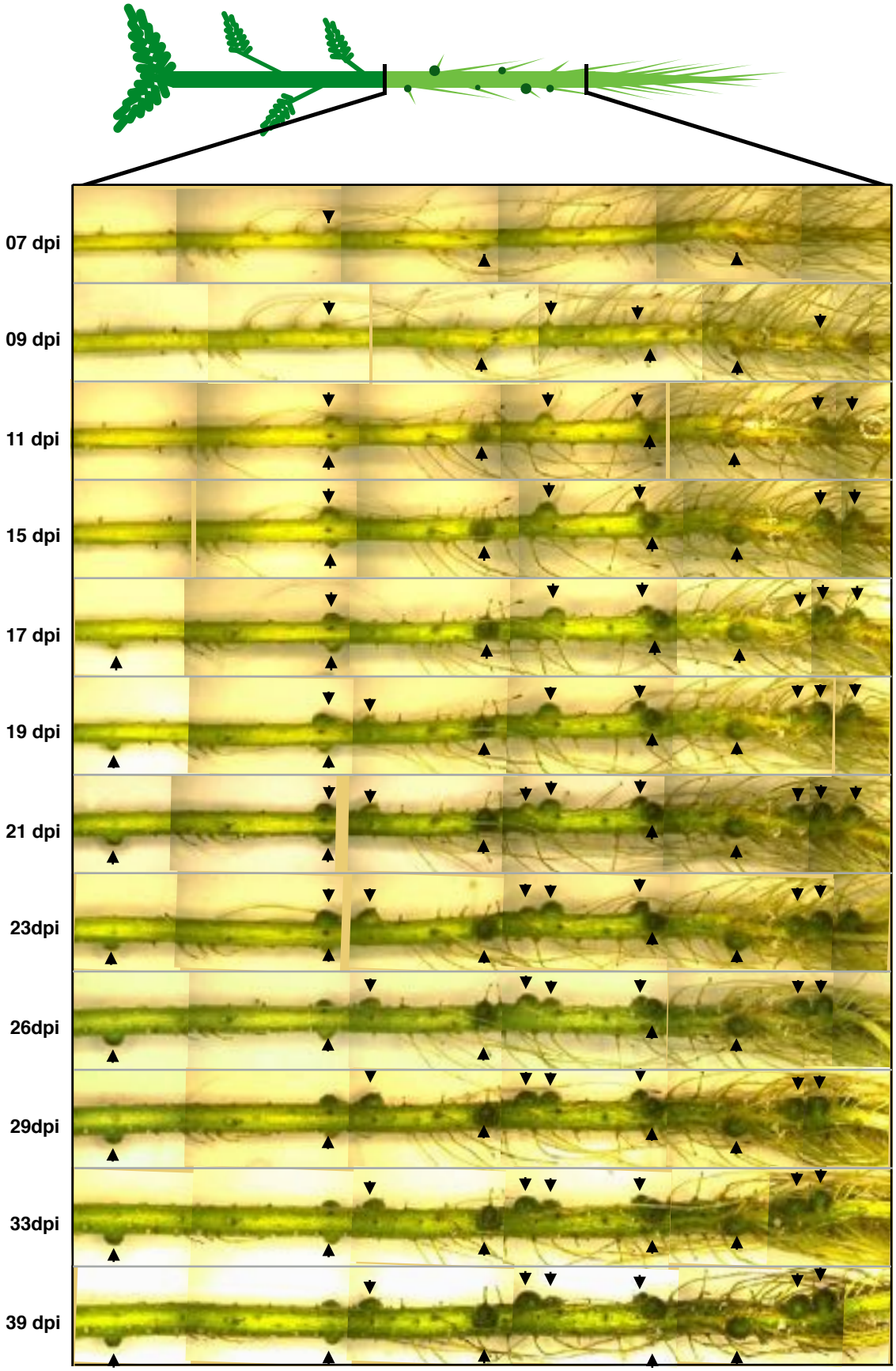

Figure S4. Reconstructed images of the root system of a wild type-infected *A. afraspera* plant. Nodules fully visible in at least five time points are indicated with black arrowheads.

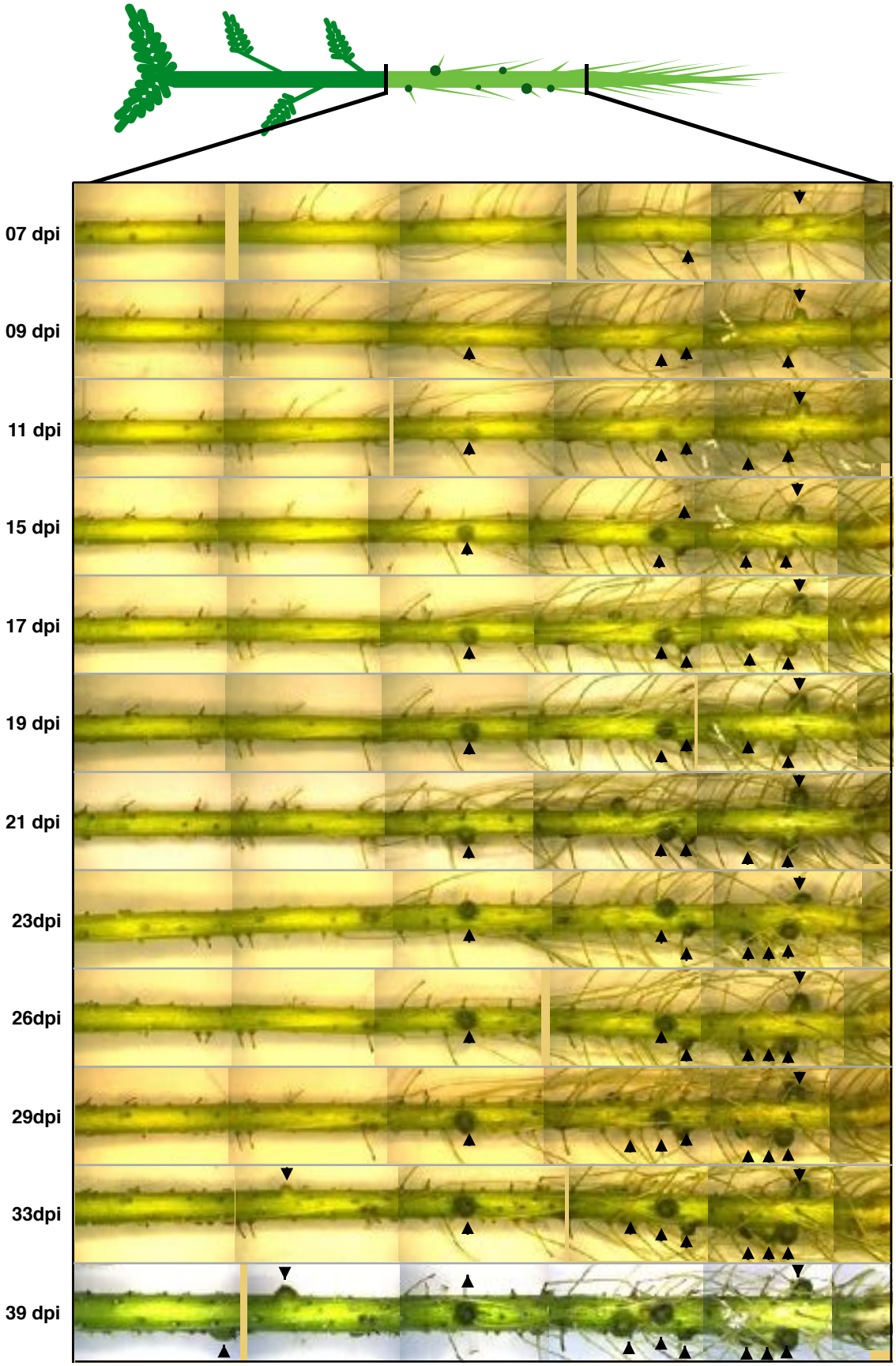

Figure S5. Reconstructed images of the root system of a Δ*hpnH*-infected *A. afraspera* plant. Nodules fully visible in at least five time points are indicated with black arrowheads.

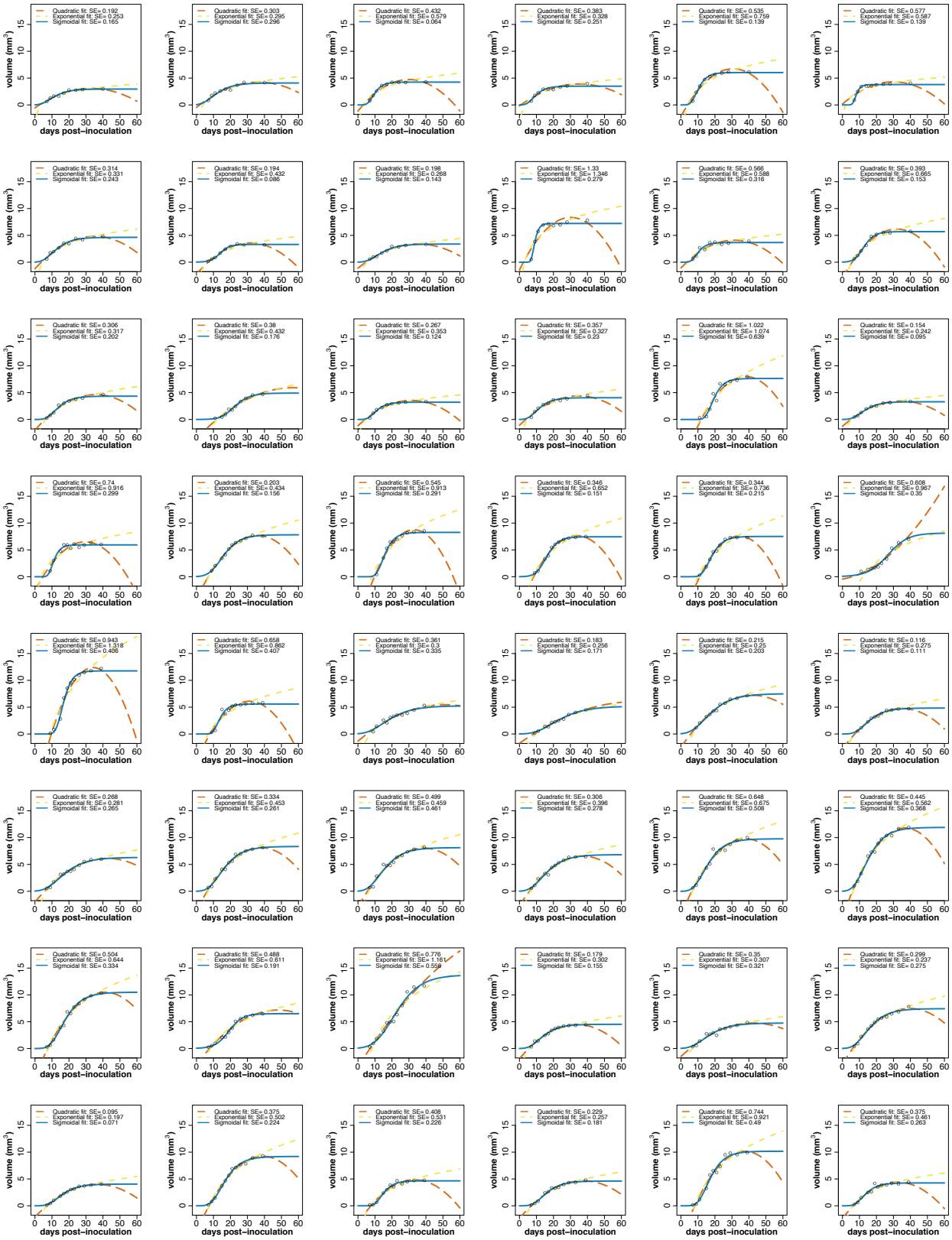
Quadratic fit: SE= 0.192
Exponential fit: SE= 0.253
Sigmoidal fit: SE= 0.165
Quadratic fit: SE= 0.303
Exponential fit: SE= 0.295
Sigmoidal fit: SE= 0.296
Quadratic fit: SE= 0.432
Exponential fit: SE= 0.579
Sigmoidal fit: SE= 0.064
Quadratic fit: SE= 0.383
Exponential fit: SE= 0.328
Sigmoidal fit: SE= 0.251
Quadratic fit: SE= 0.535
Exponential fit: SE= 0.759
Sigmoidal fit: SE= 0.139
Quadratic fit: SE= 0.577
Exponential fit: SE= 0.587
Sigmoidal fit: SE= 0.139
Quadratic fit: SE= 0.314
Exponential fit: SE= 0.331
Sigmoidal fit: SE= 0.243
Quadratic fit: SE= 0.194
Exponential fit: SE= 0.432
Sigmoidal fit: SE= 0.086
Quadratic fit: SE= 0.198
Exponential fit: SE= 0.268
Sigmoidal fit: SE= 0.143
Quadratic fit: SE= 1.33
Exponential fit: SE= 1.346
Sigmoidal fit: SE= 0.279
Quadratic fit: SE= 0.566
Exponential fit: SE= 0.588
Sigmoidal fit: SE= 0.316
Quadratic fit: SE= 0.393
Exponential fit: SE= 0.665
Sigmoidal fit: SE= 0.153
Quadratic fit: SE= 0.306
Exponential fit: SE= 0.317
Sigmoidal fit: SE= 0.202
Quadratic fit: SE= 0.38
Exponential fit: SE= 0.432
Sigmoidal fit: SE= 0.176
Quadratic fit: SE= 0.267
Exponential fit: SE= 0.353
Sigmoidal fit: SE= 0.124
Quadratic fit: SE= 0.357
Exponential fit: SE= 0.327
Sigmoidal fit: SE= 0.23
Quadratic fit: SE= 1.022
Exponential fit: SE= 1.074
Sigmoidal fit: SE= 0.639
Quadratic fit: SE= 0.154
Exponential fit: SE= 0.242
Sigmoidal fit: SE= 0.095
Quadratic fit: SE= 0.74
Exponential fit: SE= 0.916
Sigmoidal fit: SE= 0.299
Quadratic fit: SE= 0.203
Exponential fit: SE= 0.434
Sigmoidal fit: SE= 0.156
Quadratic fit: SE= 0.545
Exponential fit: SE= 0.913
Sigmoidal fit: SE= 0.291
Quadratic fit: SE= 0.346
Exponential fit: SE= 0.552
Sigmoidal fit: SE= 0.151
Quadratic fit: SE= 0.344
Exponential fit: SE= 0.736
Sigmoidal fit: SE= 0.215
Quadratic fit: SE= 0.608
Exponential fit: SE= 0.967
Sigmoidal fit: SE= 0.35
Quadratic fit: SE= 0.943
Exponential fit: SE= 1.318
Sigmoidal fit: SE= 0.406
Quadratic fit: SE= 0.658
Exponential fit: SE= 0.862
Sigmoidal fit: SE= 0.407
Quadratic fit: SE= 0.361
Exponential fit: SE= 0.3
Sigmoidal fit: SE= 0.335
Quadratic fit: SE= 0.183
Exponential fit: SE= 0.256
Sigmoidal fit: SE= 0.171
Quadratic fit: SE= 0.215
Exponential fit: SE= 0.25
Sigmoidal fit: SE= 0.203
Quadratic fit: SE= 0.116
Exponential fit: SE= 0.275
Sigmoidal fit: SE= 0.111
Quadratic fit: SE= 0.268
Exponential fit: SE= 0.281
Sigmoidal fit: SE= 0.265
Quadratic fit: SE= 0.334
Exponential fit: SE= 0.453
Sigmoidal fit: SE= 0.261
Quadratic fit: SE= 0.499
Exponential fit: SE= 0.459
Sigmoidal fit: SE= 0.461
Quadratic fit: SE= 0.306
Exponential fit: SE= 0.386
Sigmoidal fit: SE= 0.278
Quadratic fit: SE= 0.648
Exponential fit: SE= 0.675
Sigmoidal fit: SE= 0.508
Quadratic fit: SE= 0.445
Exponential fit: SE= 0.582
Sigmoidal fit: SE= 0.368
Quadratic fit: SE= 0.504
Exponential fit: SE= 0.644
Sigmoidal fit: SE= 0.334
Quadratic fit: SE= 0.488
Exponential fit: SE= 0.611
Sigmoidal fit: SE= 0.191
Quadratic fit: SE= 0.776
Exponential fit: SE= 1.161
Sigmoidal fit: SE= 0.558
Quadratic fit: SE= 0.179
Exponential fit: SE= 0.302
Sigmoidal fit: SE= 0.155
Quadratic fit: SE= 0.35
Exponential fit: SE= 0.307
Sigmoidal fit: SE= 0.321
Quadratic fit: SE= 0.299
Exponential fit: SE= 0.237
Sigmoidal fit: SE= 0.275
Quadratic fit: SE= 0.095
Exponential fit: SE= 0.197
Sigmoidal fit: SE= 0.071
Quadratic fit: SE= 0.375
Exponential fit: SE= 0.502
Sigmoidal fit: SE= 0.224
Quadratic fit: SE= 0.408
Exponential fit: SE= 0.531
Sigmoidal fit: SE= 0.226
Quadratic fit: SE= 0.229
Exponential fit: SE= 0.257
Sigmoidal fit: SE= 0.181
Quadratic fit: SE= 0.744
Exponential fit: SE= 0.921
Sigmoidal fit: SE= 0.49
Quadratic fit: SE= 0.375
Exponential fit: SE= 0.461
Sigmoidal fit: SE= 0.263
volume (mm3)
days post−inoculation

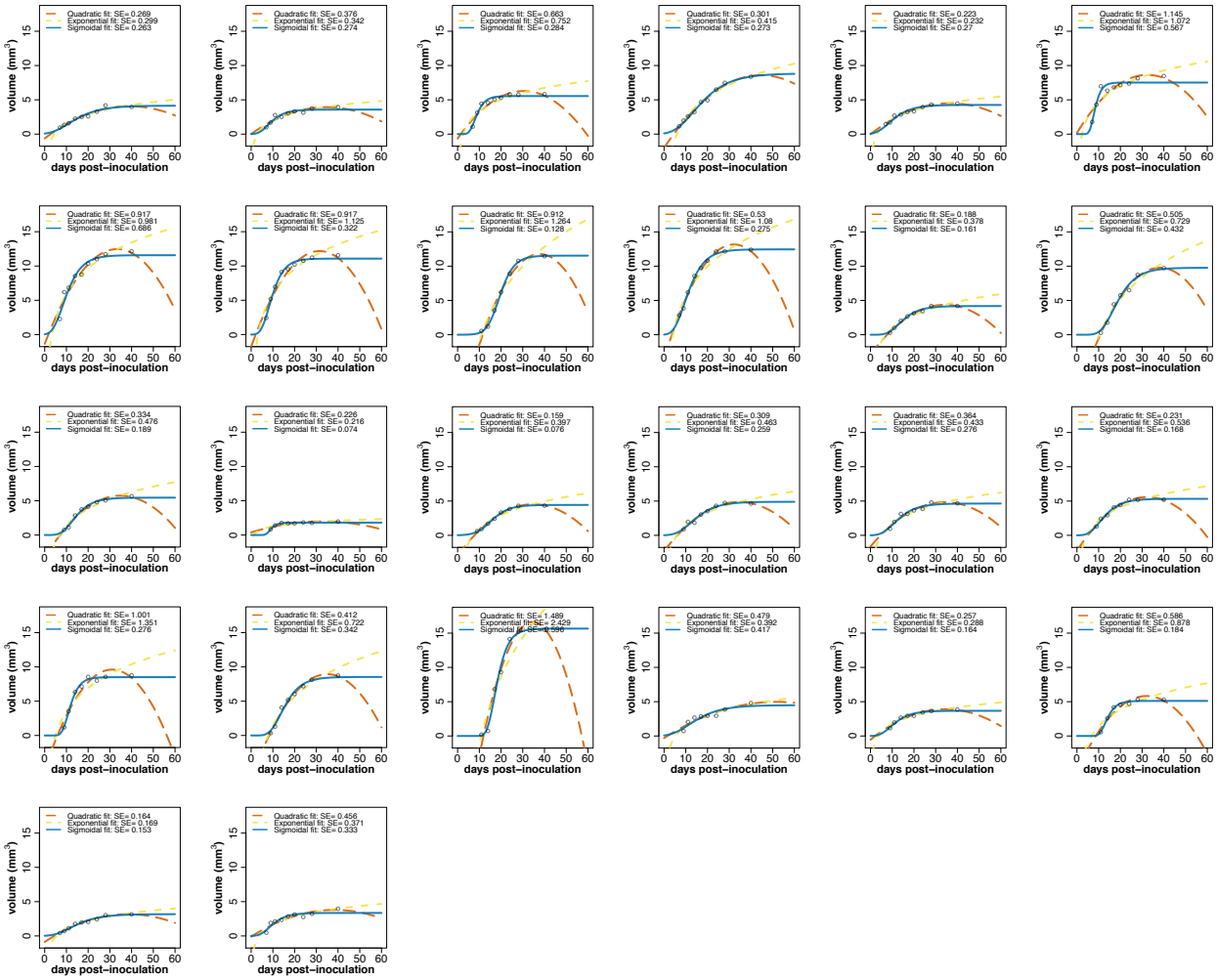

Figure S6. Nodule growth plots for all 74 wild type-infected nodules fit with quadratic (orange; long dashed lines), exponential (yellow; short dashed lines), or sigmoidal (blue; solid lines) models. Standard errors (SE) for each model are shown.

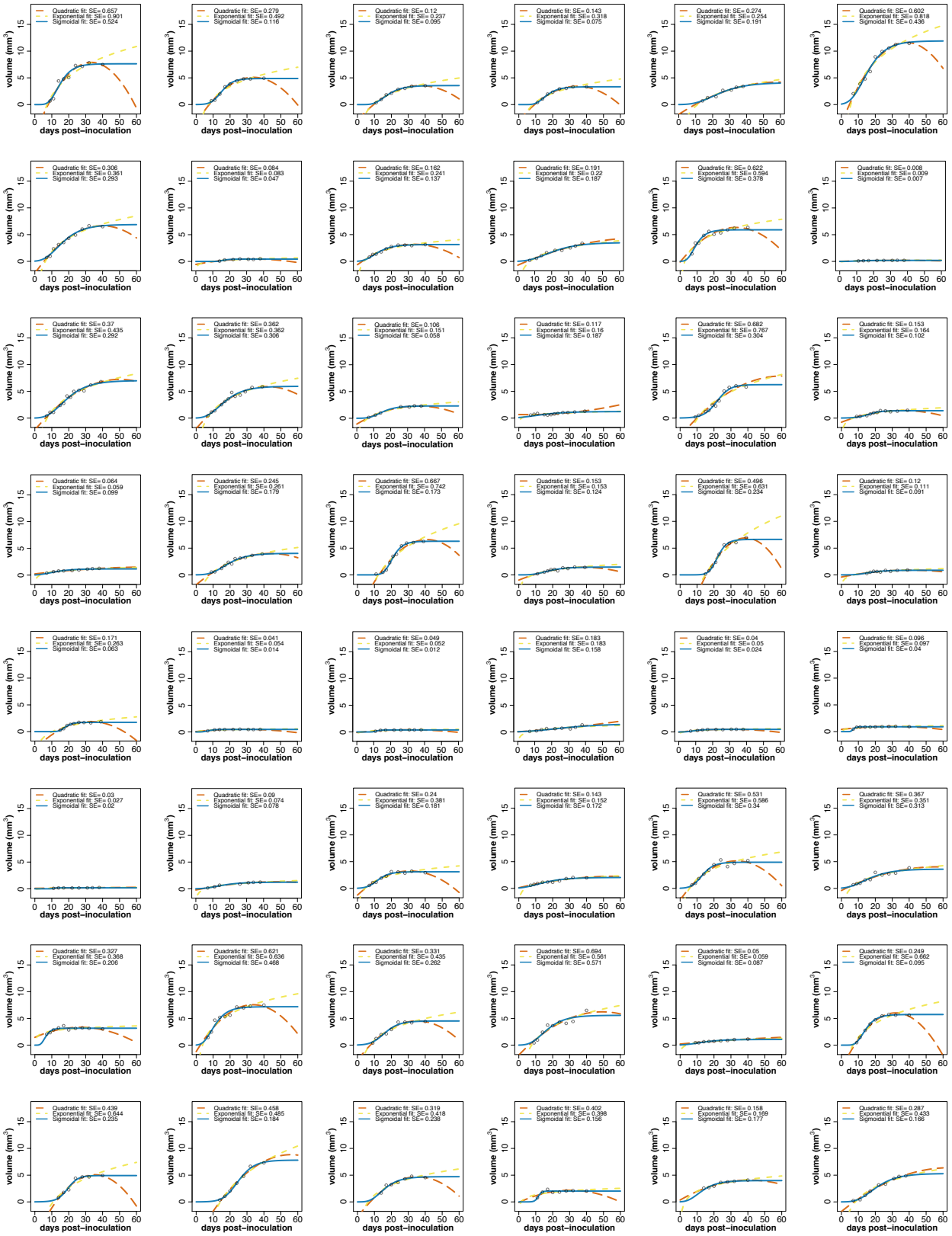
Quadratic fit: SE= 0.657
Exponential fit: SE= 0.901
Sigmoidal fit: SE= 0.524
Quadratic fit: SE= 0.279
Exponential fit: SE= 0.492
Sigmoidal fit: SE= 0.116
Quadratic fit: SE= 0.12
Exponential fit: SE= 0.237
Sigmoidal fit: SE= 0.095
Quadratic fit: SE= 0.143
Exponential fit: SE= 0.318
Sigmoidal fit: SE= 0.075
Quadratic fit: SE= 0.274
Exponential fit: SE= 0.254
Sigmoidal fit: SE= 0.191
Quadratic fit: SE= 0.602
Exponential fit: SE= 0.818
Sigmoidal fit: SE= 0.436
Quadratic fit: SE= 0.306
Exponential fit: SE= 0.361
Sigmoidal fit: SE= 0.293
Quadratic fit: SE= 0.084
Exponential fit: SE= 0.083
Sigmoidal fit: SE= 0.047
Quadratic fit: SE= 0.162
Exponential fit: SE= 0.241
Sigmoidal fit: SE= 0.137
Quadratic fit: SE= 0.191
Exponential fit: SE= 0.22
Sigmoidal fit: SE= 0.187
Quadratic fit: SE= 0.622
Exponential fit: SE= 0.594
Sigmoidal fit: SE= 0.378
Quadratic fit: SE= 0.008
Exponential fit: SE= 0.009
Sigmoidal fit: SE= 0.007
Quadratic fit: SE= 0.37
Exponential fit: SE= 0.435
Sigmoidal fit: SE= 0.292
Quadratic fit: SE= 0.362
Exponential fit: SE= 0.362
Sigmoidal fit: SE= 0.306
Quadratic fit: SE= 0.106
Exponential fit: SE= 0.151
Sigmoidal fit: SE= 0.058
Quadratic fit: SE= 0.117
Exponential fit: SE= 0.16
Sigmoidal fit: SE= 0.187
Quadratic fit: SE= 0.682
Exponential fit: SE= 0.767
Sigmoidal fit: SE= 0.304
Quadratic fit: SE= 0.153
Exponential fit: SE= 0.164
Sigmoidal fit: SE= 0.102
Quadratic fit: SE= 0.064
Exponential fit: SE= 0.059
Sigmoidal fit: SE= 0.099
Quadratic fit: SE= 0.245
Exponential fit: SE= 0.261
Sigmoidal fit: SE= 0.179
Quadratic fit: SE= 0.667
Exponential fit: SE= 0.742
Sigmoidal fit: SE= 0.173
Quadratic fit: SE= 0.153
Exponential fit: SE= 0.153
Sigmoidal fit: SE= 0.124
Quadratic fit: SE= 0.496
Exponential fit: SE= 0.631
Sigmoidal fit: SE= 0.234
Quadratic fit: SE= 0.12
Exponential fit: SE= 0.111
Sigmoidal fit: SE= 0.091
Quadratic fit: SE= 0.171
Exponential fit: SE= 0.263
Sigmoidal fit: SE= 0.063
Quadratic fit: SE= 0.041
Exponential fit: SE= 0.054
Sigmoidal fit: SE= 0.014
Quadratic fit: SE= 0.049
Exponential fit: SE= 0.052
Sigmoidal fit: SE= 0.012
Quadratic fit: SE= 0.183
Exponential fit: SE= 0.183
Sigmoidal fit: SE= 0.158
Quadratic fit: SE= 0.04
Exponential fit: SE= 0.05
Sigmoidal fit: SE= 0.024
Quadratic fit: SE= 0.096
Exponential fit: SE= 0.097
Sigmoidal fit: SE= 0.04
Quadratic fit: SE= 0.03
Exponential fit: SE= 0.027
Sigmoidal fit: SE= 0.02
Quadratic fit: SE= 0.09
Exponential fit: SE= 0.074
Sigmoidal fit: SE= 0.078
Quadratic fit: SE= 0.24
Exponential fit: SE= 0.381
Sigmoidal fit: SE= 0.181
Quadratic fit: SE= 0.143
Exponential fit: SE= 0.152
Sigmoidal fit: SE= 0.172
Quadratic fit: SE= 0.531
Exponential fit: SE= 0.586
Sigmoidal fit: SE= 0.34
Quadratic fit: SE= 0.367
Exponential fit: SE= 0.351
Sigmoidal fit: SE= 0.313
Quadratic fit: SE= 0.327
Exponential fit: SE= 0.368
Sigmoidal fit: SE= 0.206
Quadratic fit: SE= 0.621
Exponential fit: SE= 0.636
Sigmoidal fit: SE= 0.468
Quadratic fit: SE= 0.331
Exponential fit: SE= 0.435
Sigmoidal fit: SE= 0.262
Quadratic fit: SE= 0.694
Exponential fit: SE= 0.561
Sigmoidal fit: SE= 0.571
Quadratic fit: SE= 0.05
Exponential fit: SE= 0.059
Sigmoidal fit: SE= 0.087
Quadratic fit: SE= 0.249
Exponential fit: SE= 0.662
Sigmoidal fit: SE= 0.095
Quadratic fit: SE= 0.439
Exponential fit: SE= 0.644
Sigmoidal fit: SE= 0.235
Quadratic fit: SE= 0.458
Exponential fit: SE= 0.485
Sigmoidal fit: SE= 0.184
Quadratic fit: SE= 0.319
Exponential fit: SE= 0.418
Sigmoidal fit: SE= 0.238
Quadratic fit: SE= 0.402
Exponential fit: SE= 0.398
Sigmoidal fit: SE= 0.156
Quadratic fit: SE= 0.158
Exponential fit: SE= 0.169
Sigmoidal fit: SE= 0.177
Quadratic fit: SE= 0.287
Exponential fit: SE= 0.433
Sigmoidal fit: SE= 0.166
volume (mm^3)
days post−inoculation

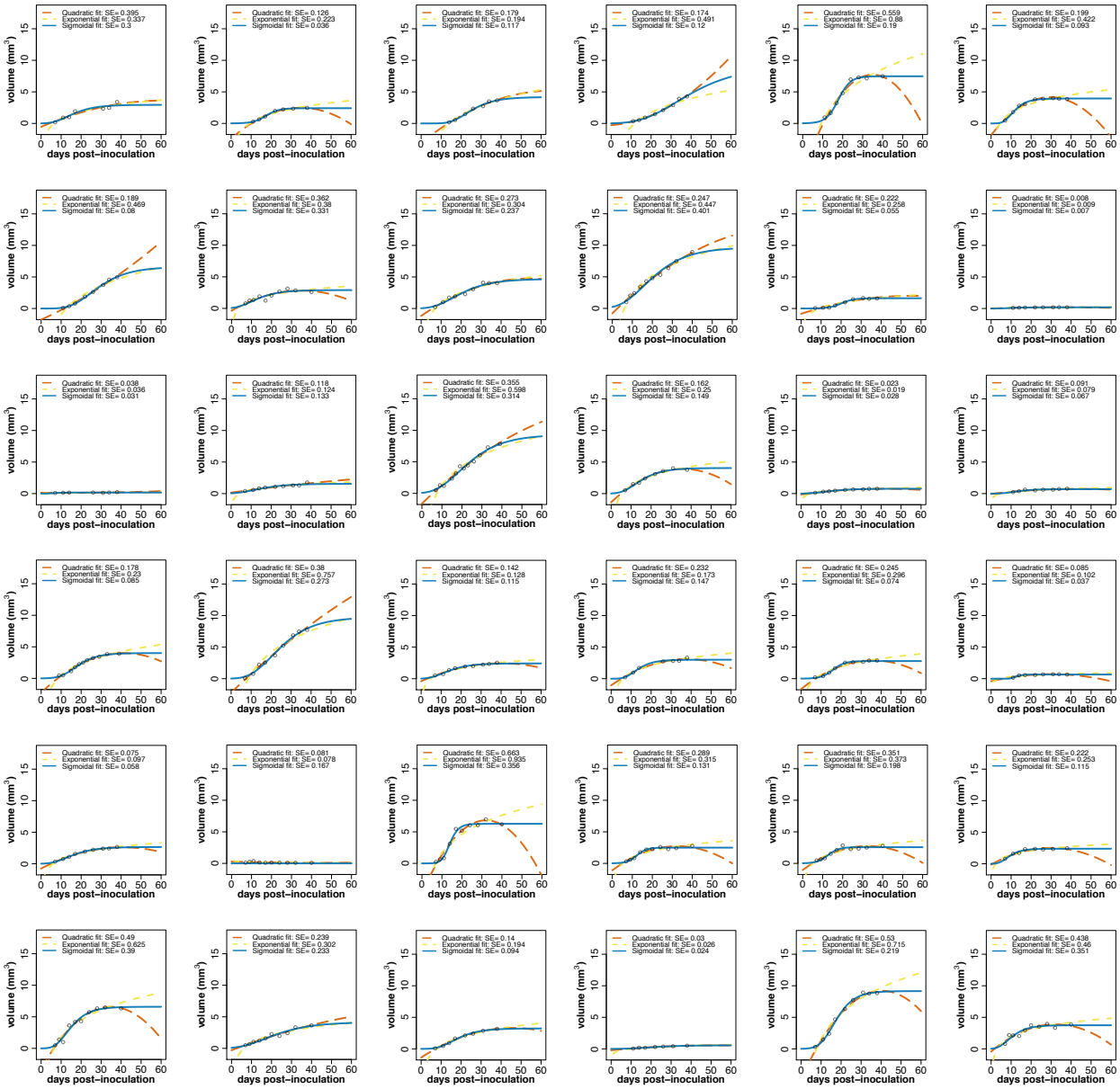

Figure S7. Nodule growth plots for all 84 Δ*hpnH*-infected nodules fit with quadratic (orange; long dashed lines), exponential (yellow; short dashed lines), or sigmoidal (blue; solid lines) models. Standard errors (SE) for each model are shown.

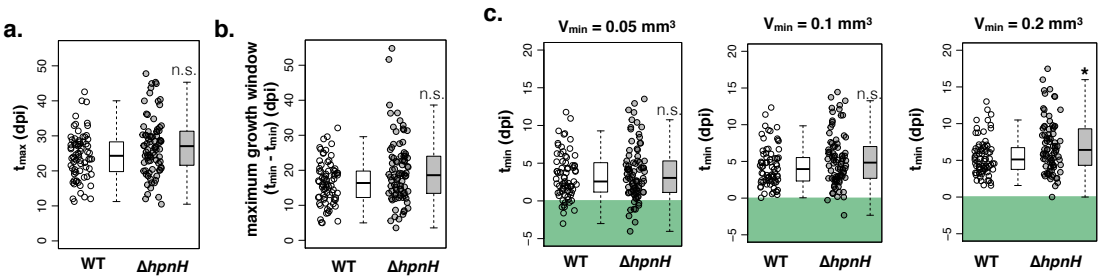

Figure S8. (**a**) Jitter and box plots of $\mathbf{t_{max}}$ values for all wild type- and Δ*hpnH*-infected nodules. (**b**) Jitter and box plots of maximum growth windows for all wild type- and Δ*hpnH*-infected nodules. (**c**) Jitter and box plots of $\mathbf{t_{min}}$ values (as determined by extrapolation using sigmoidal fits of nodule growth curves) for all wild type- and Δ*hpnH*-infected nodules, in which $\mathbf{V_{min}}$ is defined as 0.05 mm^3, 0.1 mm^3, 0.2 mm^3. Green shading highlights negative $\mathbf{t_{min}}$ values. Results of KS-tests between wild-type and Δ*hpnH* nodules are denoted as follows: *, $p<0.05$; n.s., $p>0.05$.

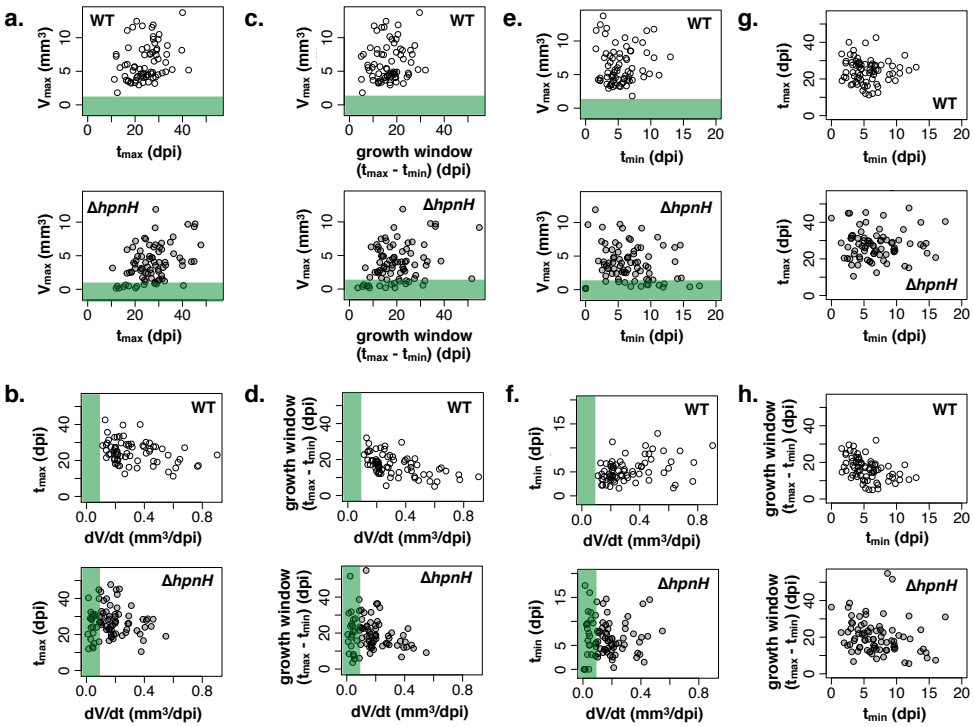

Figure S9. (**a-b**) Scatter plots of $\mathbf{t_{max}}$ vs. (**a**) **dV/dt** and (**b**) $\mathbf{V_{max}}$ for all wild type- (open circles) and Δ*hpnH*- (grey circles) infected nodules. Green regions highlight values below what is observed for wild type. (**c-d**) Scatter plots of maximum growth windows vs. (**c**) **dV/dt** and (**d**) $\mathbf{V_{max}}$. (**e-f**) Scatter plots of $\mathbf{t_{min}}$ vs. (**c**) **dV/dt** and (**d**) $\mathbf{V_{max}}$. (**g-h**) Scatter plots of $\mathbf{t_{min}}$ vs. (**a**) $\mathbf{t_{max}}$ and (**b**) maximum growth windows.

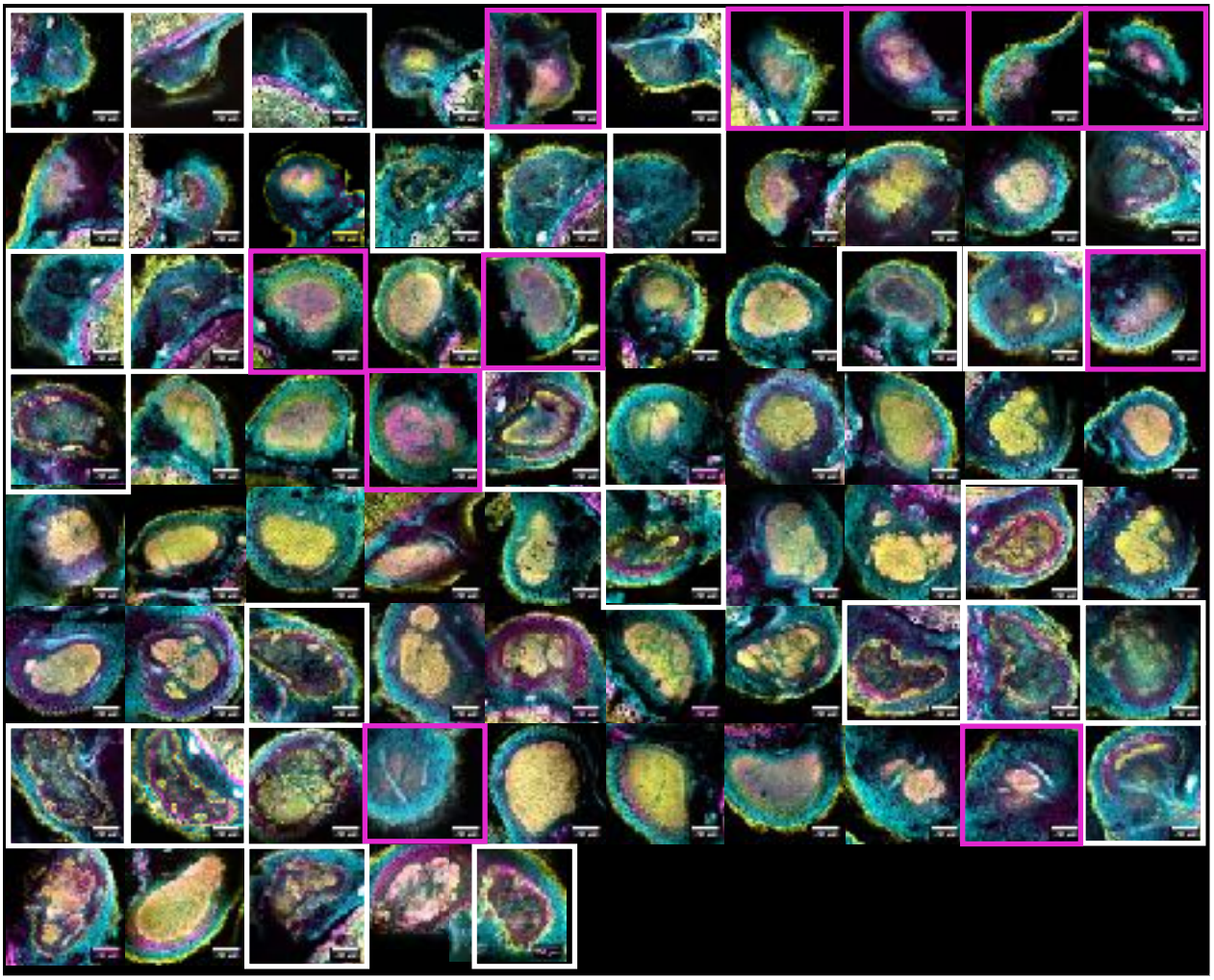

Figure S10. Confocal sections of small (<0.5 mm radius) Δ*hpnH*-infected nodules harvested at 40 dpi. Sections were stained with Calcofluor (cyan), SYTO9 (yellow), and propidium iodide (magenta). N=74 nodules harvested from 5 plants. White boxes highlight under-infected nodules. Magenta boxes indicate nodules primarily containing membrane-compromised cells.

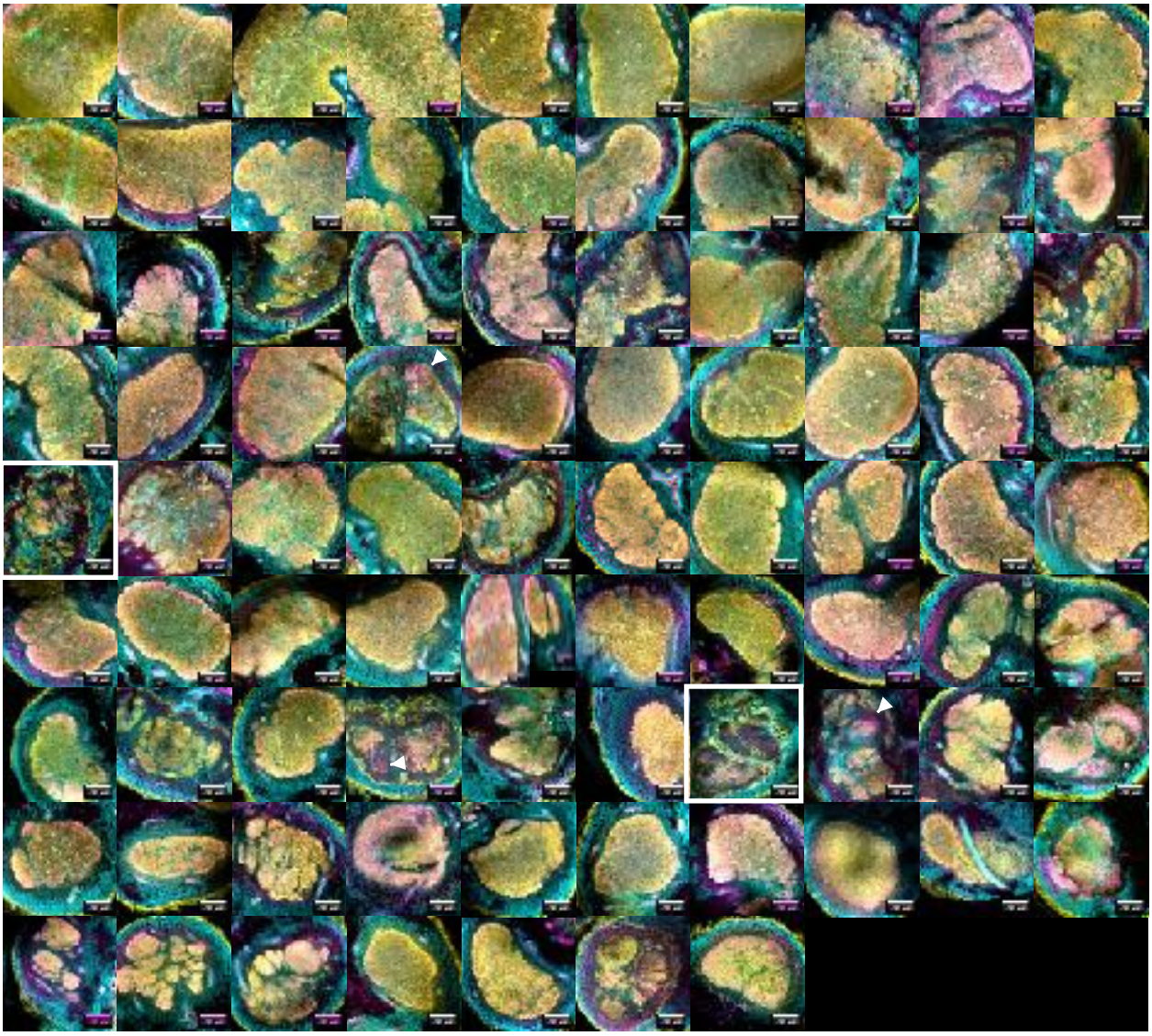

Figure S11. Confocal sections of large (>0.5 mm radius) Δ*hpnH*-infected nodules harvested at 40 dpi. Sections were stained with Calcofluor (cyan), SYTO9 (yellow), and propidium iodide (magenta). N=87 nodules harvested from 5 plants. White boxes highlight under-infected nodules.

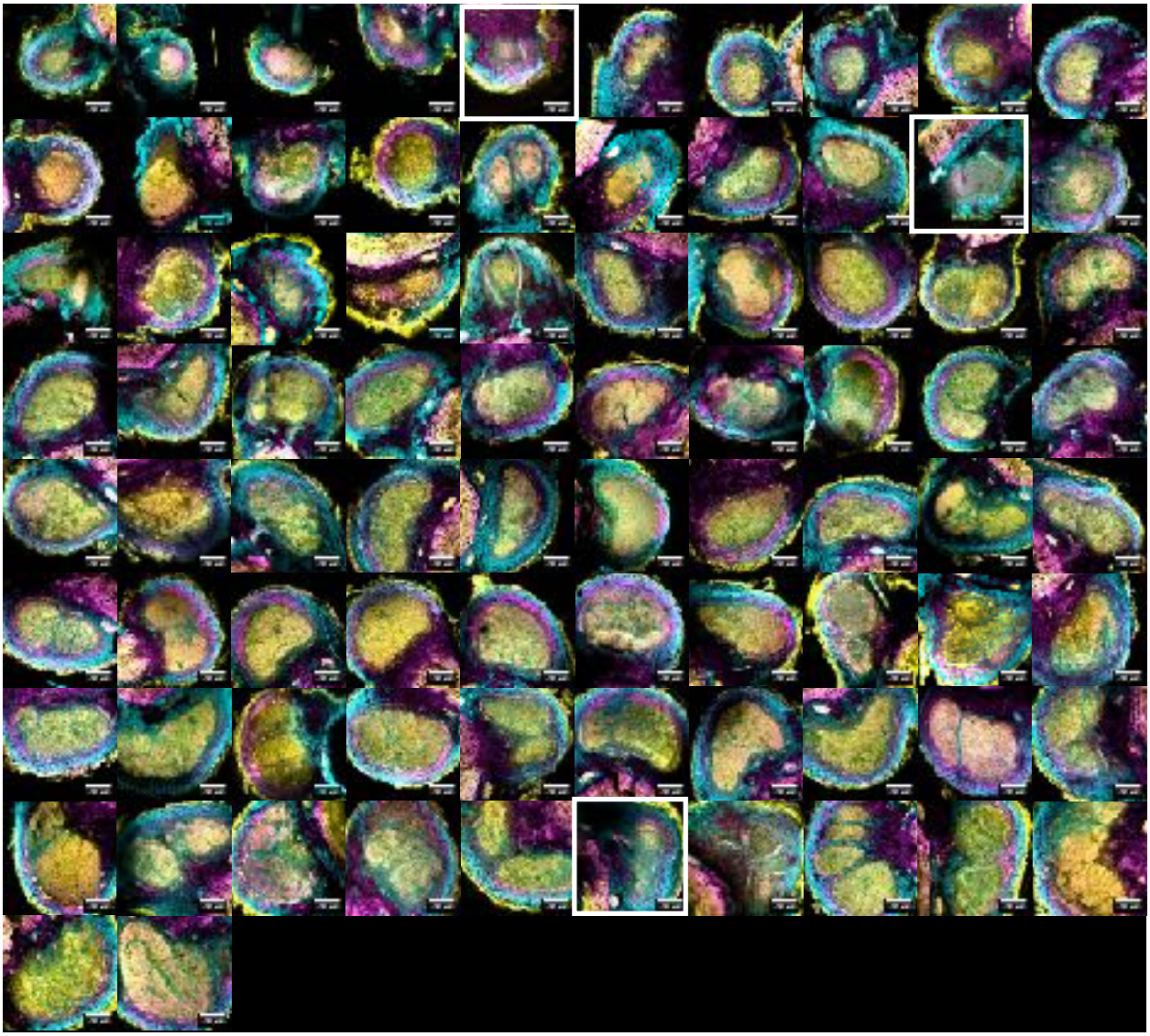

Figure S12. Confocal sections of small (<0.5 mm radius) wild type-infected nodules harvested at 10 dpi. Sections were stained with Calcofluor (cyan), SYTO9 (yellow), and propidium iodide (magenta). N=80 nodules harvested from 5 plants. White boxes highlight under-infected nodules.

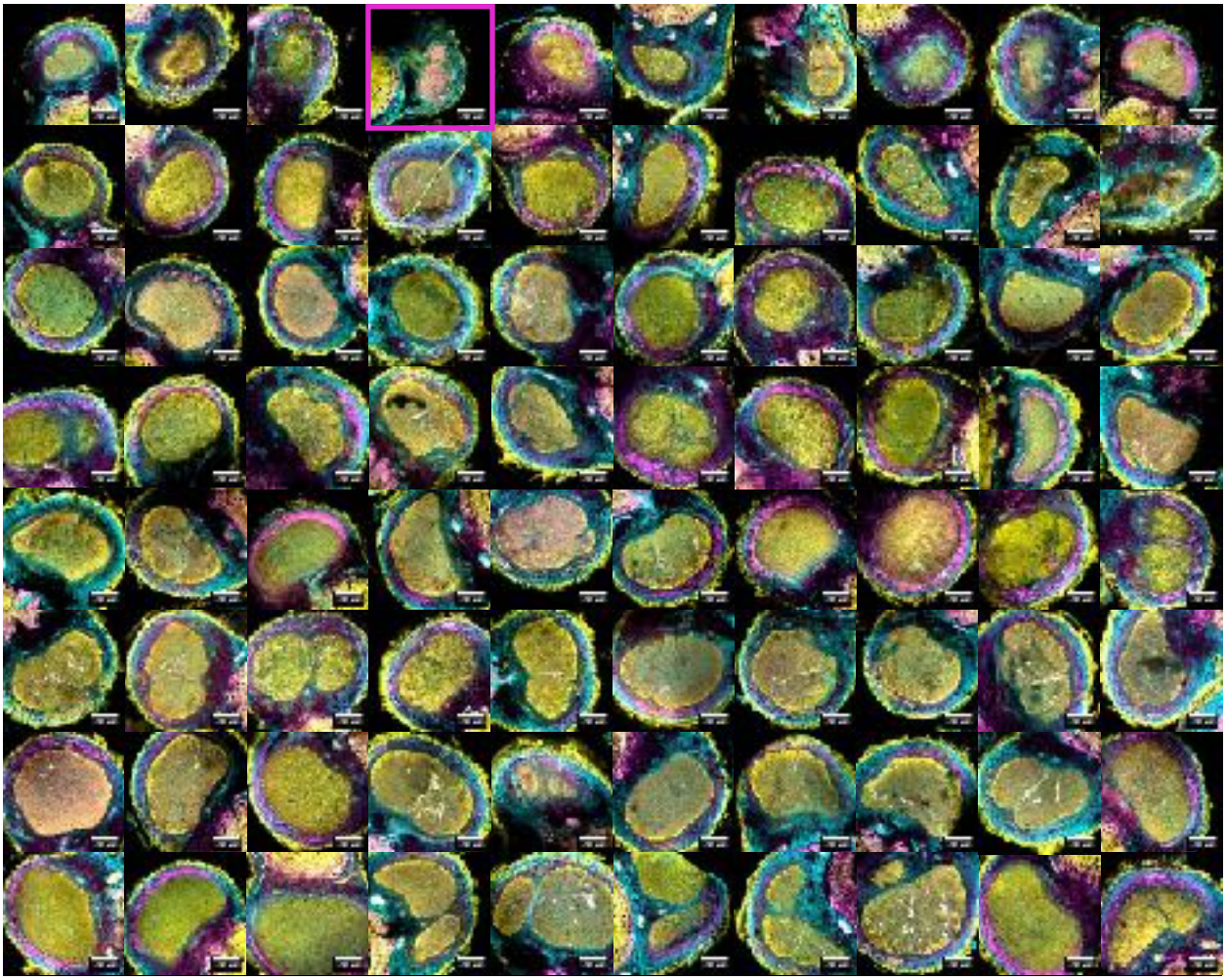

Figure S13. Confocal sections of small (<0.5 mm radius) wild type-infected nodules harvested at 25 dpi. Sections were stained with Calcofluor (cyan), SYTO9 (yellow), and propidium iodide (magenta). N=82 nodules harvested from 5 plants. Magenta boxes indicate nodules primarily containing membrane-compromised cells.

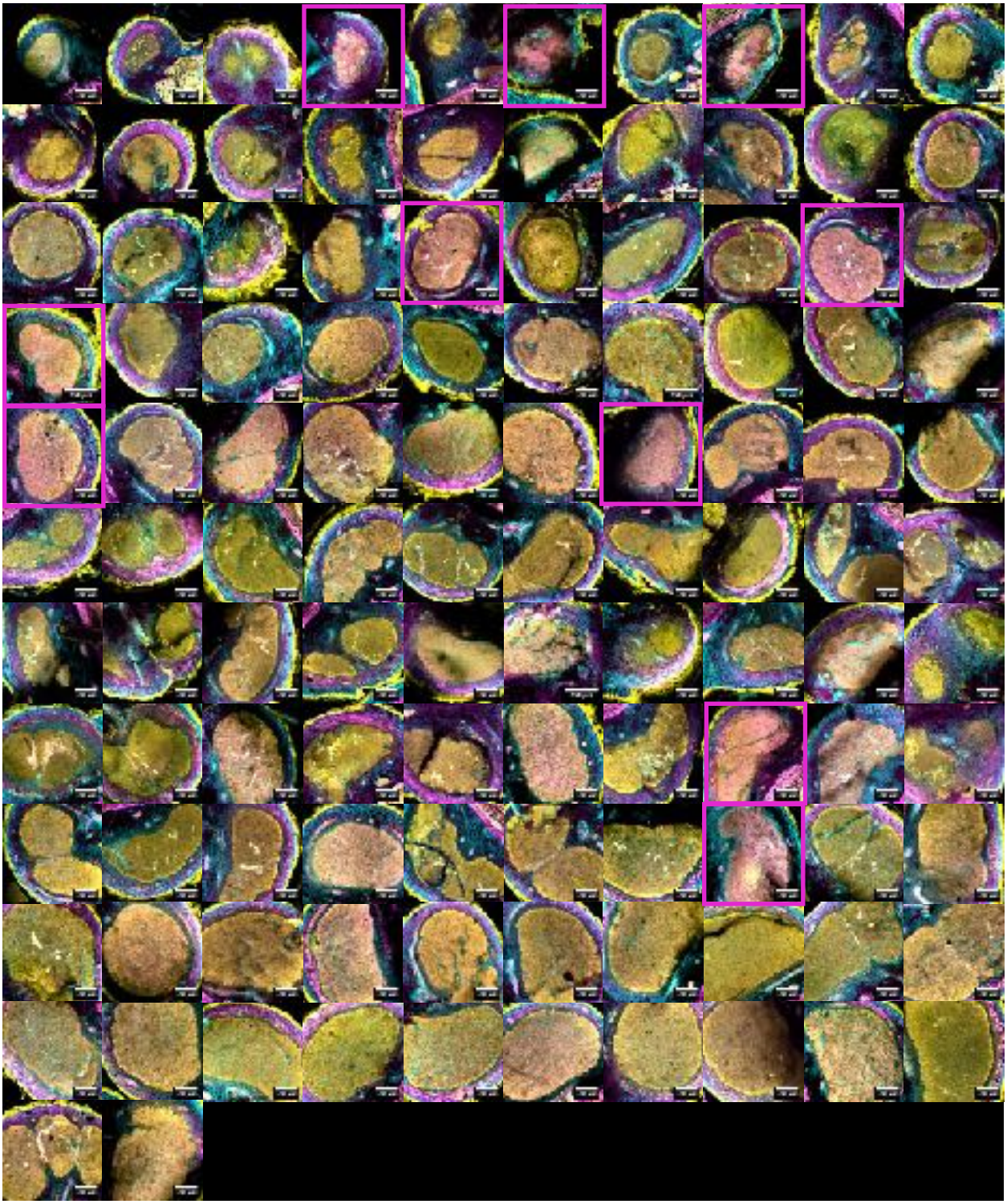

Figure S14. Confocal sections of wild type-infected nodules harvested at 40 dpi. Sections were stained with Calcofluor (cyan), SYTO9 (yellow), and propidium iodide (magenta). N=117 nodules harvested from 5 plants. Magenta boxes indicate nodules primarily containing membrane-compromised cells.

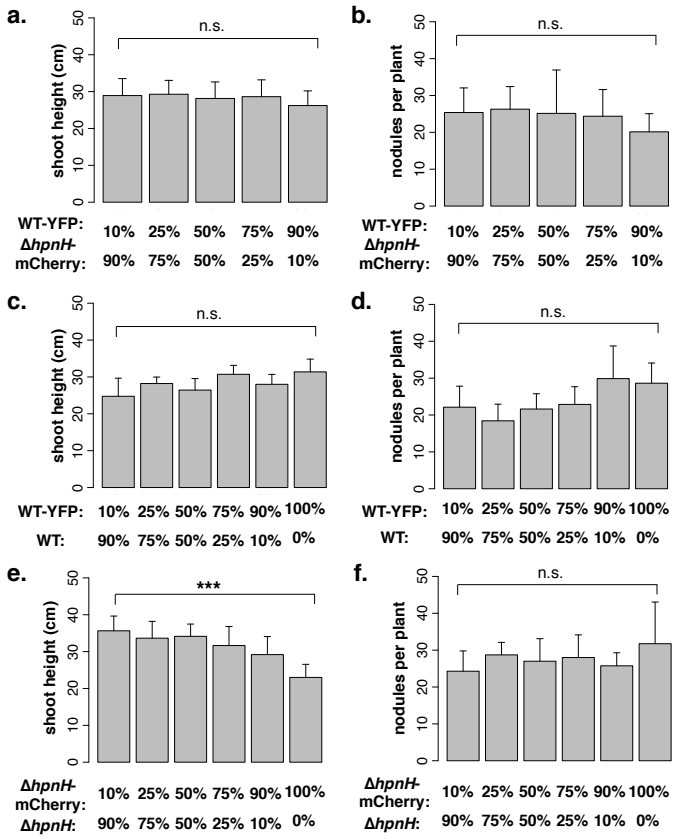

Figure S15. Average shoot height (**a**) and number of nodules (**b**) for plants co-inoculated with Δ*hpnH*-mCherry and WT-YFP strains, recorded at 45 dpi. Average shoot height (**c**) and number of nodules (**d**) for plants co-inoculated with WT and WT-YFP strains, recorded at 40 dpi. Average shoot height (**e**) and number of nodules (**f**) for plants co-inoculated with Δ*hpnH* and Δ*hpnH*-mCherry strains, recorded at 50 dpi. N=7-8 plants per bar for all panels. Error bars represent one standard deviation. Results of two-tailed t-tests are denoted as follows: n.s., $p>0.05$; ***, $p<0.0001$.

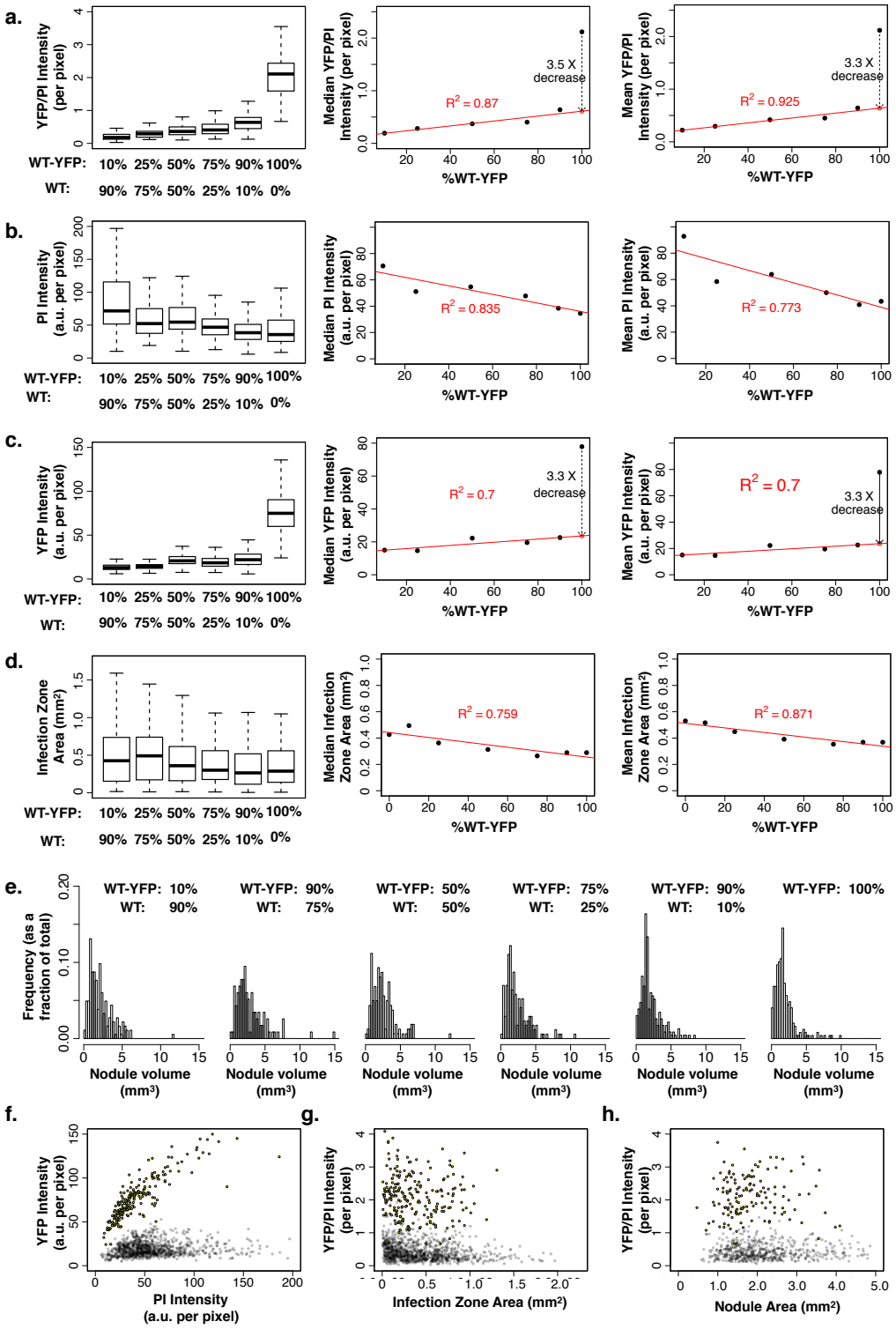

Figure S16. (**a**-**d**) Intensity ratio of YFP to mCherry (**a**), mCherry intensity (**b**), and YFP intensity (**c**) per pixel within infection zones of nodules co-inoculated with Δ*hpnH*-mCherry and WT-YFP strains. (**d**) Cross-sectional area of infection zones of nodules co-inoculated with Δ*hpnH*-mCherry and WT-YFP strains. For (**a**-**d**), N=132, 125, 143, 143 and 110 nodules for 10%, 25%, 50%, 75% and 90% WT-YFP strain mixtures, respectively, which were sectioned and fixed between 45-50 dpi. (**e**) Nodule volume distributions from plants co-inoculated with Δ*hpnH*-mCherry and WT-YFP strains at 45 dpi. Sample sizes are N = 251, 200, 227, 204, and 149 nodules pooled from N = 8, 7, 7, 8, and 7 plants for the 10%, 25%, 50%, 75% and 90% WT-YFP strain mixtures, respectively. (**f**) Scatter plots of mCherry vs. YFP intensities per pixel within infection zones of nodules co-inoculated with Δ*hpnH*-mCherry and WT-YFP strains. (**g**-**h**) Scatter plots of YFP/mCherry intensity ratios per pixel in infection zones vs. infection zone (**g**) and nodule (**h**) cross-section areas for nodules co-inoculated with Δ*hpnH*-mCherry and WT-YFP. Scatter plots contain data pooled from all ratios.

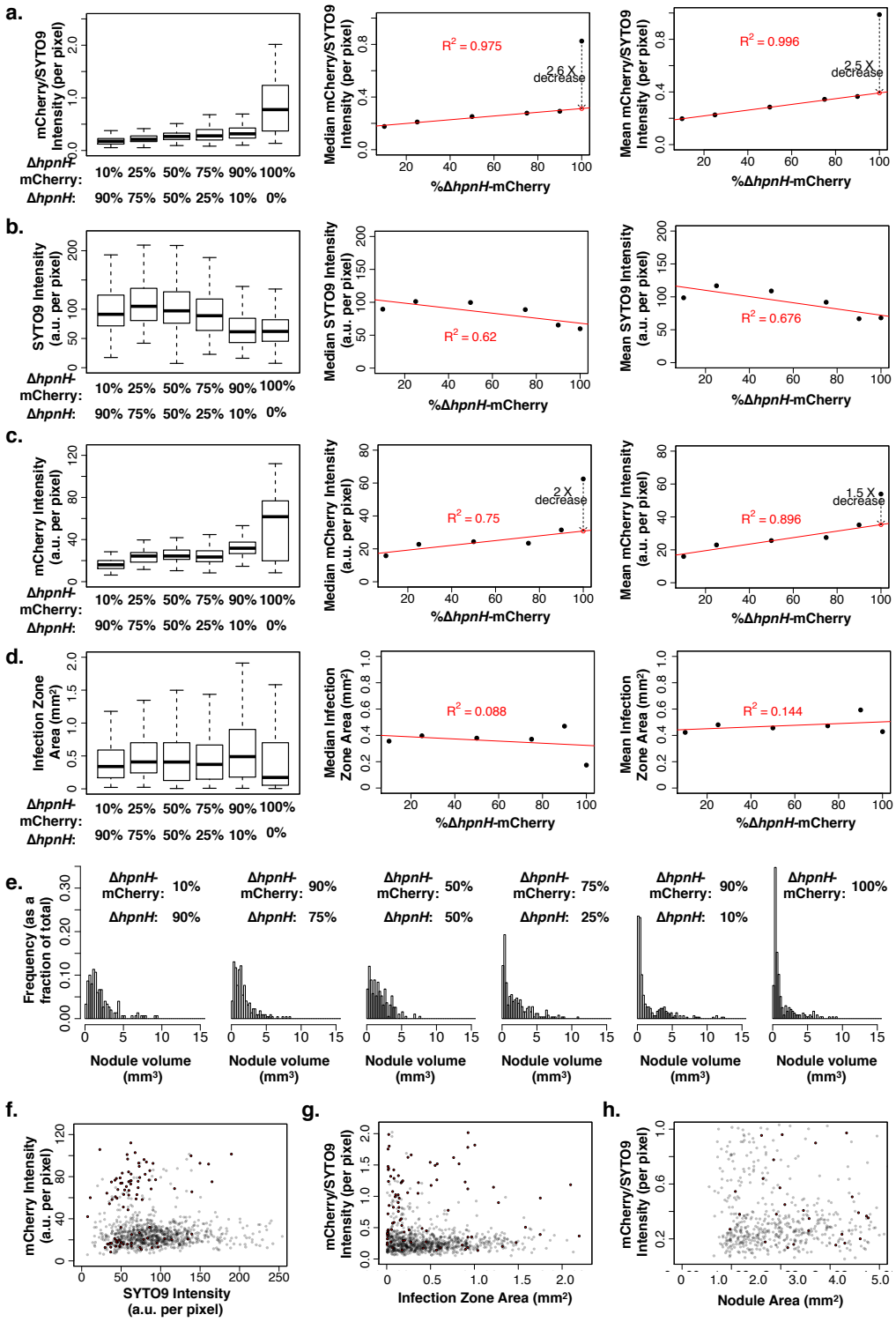

Figure S17. (**a**-**d**) Intensity ratio of YFP to propidium iodide (PI) (**a**), PI intensity (**b**), and YFP intensity (**c**) per pixel within infection zones of nodules co-inoculated with WT and WT-YFP strains. (**d**) Cross-sectional area of infection zones of nodules co-inoculated with WT and WT-YFP strains. For (**a**-**d**), N = 141, 95, 134, 147, 133, and 167 nodules for 10%, 25%, 50%, 75%, 90% and 100% WT-YFP strain mixtures, respectively, which were sectioned and fixed between 40-45 dpi. (**e**) Nodule volume distributions from plants co-inoculated with WT and WT-YFP strains at 40 dpi. Sample sizes are N = 183, 116, 161, 172, 232, and 248 nodules pooled from N = 8, 7, 8, 8, 8, and 8 plants for the 10%, 25%, 50%, 75% and 90% WT-YFP strain mixtures, respectively. (**f**) Scatter plots of PI vs. YFP intensities per pixel within infection zones of nodules co-inoculated with WT and WT-YFP strains. (**g**-**h**) Scatter plots of YFP/PI intensity ratios per pixel in infection zones vs. infection zone (**g**) and nodule (**h**) cross-section areas for nodules co-inoculated with WT and WT-YFP strains. Scatter plots contain data pooled from all ratios.

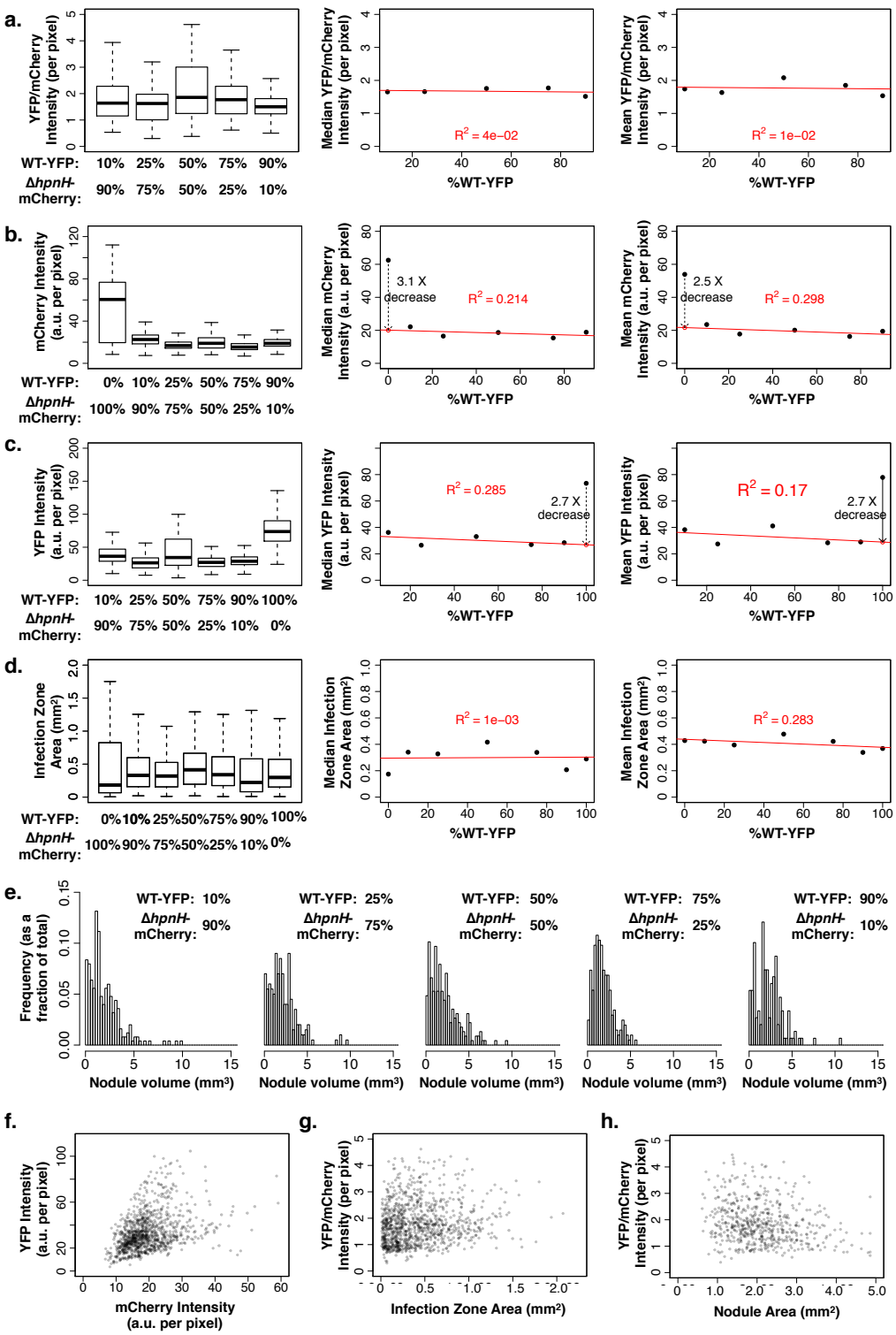

Figure S18. (**a**-**d**) Intensity ratio of mCherry to SYTO9 (**a**), SYTO9 intensity (**b**), and mCherry intensity (**c**) per pixel within infection zones of nodules co-inoculated with Δ*hpnH*-mCherry and Δ*hpnH* strains. (**d**) Cross-sectional area of infection zones of nodules co-inoculated with Δ*hpnH*-mCherry and Δ*hpnH* strains. For (**a**-**d**), N = 117, 107, 128, 137, 103 and 50 nodules for 10%, 25%, 50%, 75%, 90% and 100% Δ*hpnH*-mCherry strain mixtures, respectively, which were sectioned and fixed between 50-55 dpi. (**e**) Nodule volume distributions from plants co-inoculated with Δ*hpnH*-mCherry and Δ*hpnH* strains at 45 dpi. Sample sizes are N = 150, 222, 191, 254, 297, and 236 nodules pooled from N = 7, 7, 7, 8, 8, and 8 plants for the 10%, 25%, 50%, 75% and 90% WT-YFP strain mixtures, respectively. (**f**) Scatter plots of mCherry vs. SYTO9 intensities per pixel within infection zones of nodules co-inoculated with Δ*hpnH*-mCherry and Δ*hpnH* strains. (**g**-**h**) Scatter plots of mCherry/SYTO9 intensity ratios per pixel in infection zones vs. infection zone (**g**) and nodule (**h**) cross-section areas for nodules co-inoculated with Δ*hpnH*-mCherry and Δ*hpnH* strains. Scatter plots contain data pooled from all strain ratios.

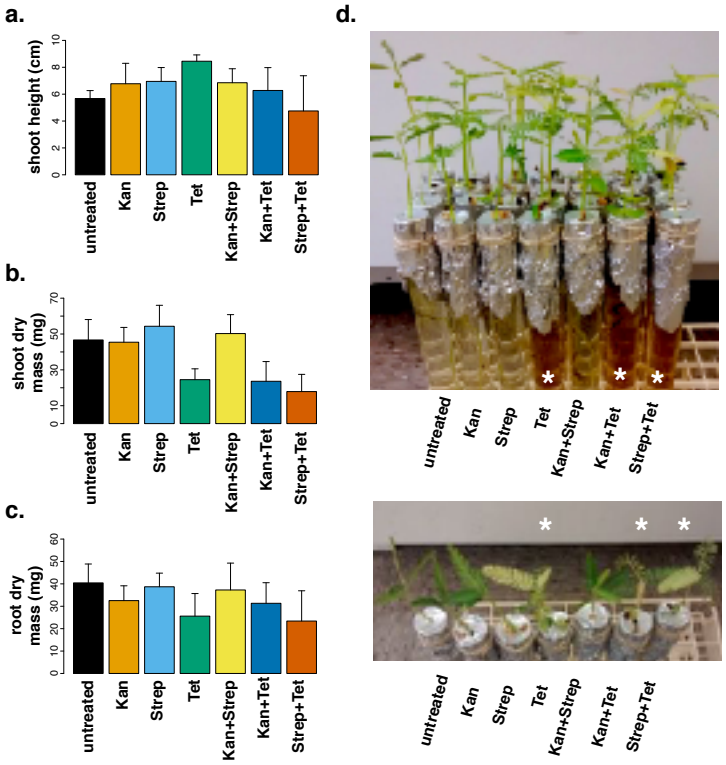

Figure S19. Average (**a**) shoot height, (**b**) shoot dry mass and (**c**) root dry mass for non-inoculated *A. afraspera* plants grown in BNM supplemented with kanamycin, streptomycin or tetracycline for 2 weeks under normal growth conditions. N=4 plants per condition; error bars represent one standard deviation. (**d-e**) Images of *A. afraspera* plants after 2 weeks of antibiotic treatment. Asterisks indicate plants grown in tetracycline-supplemented medium.

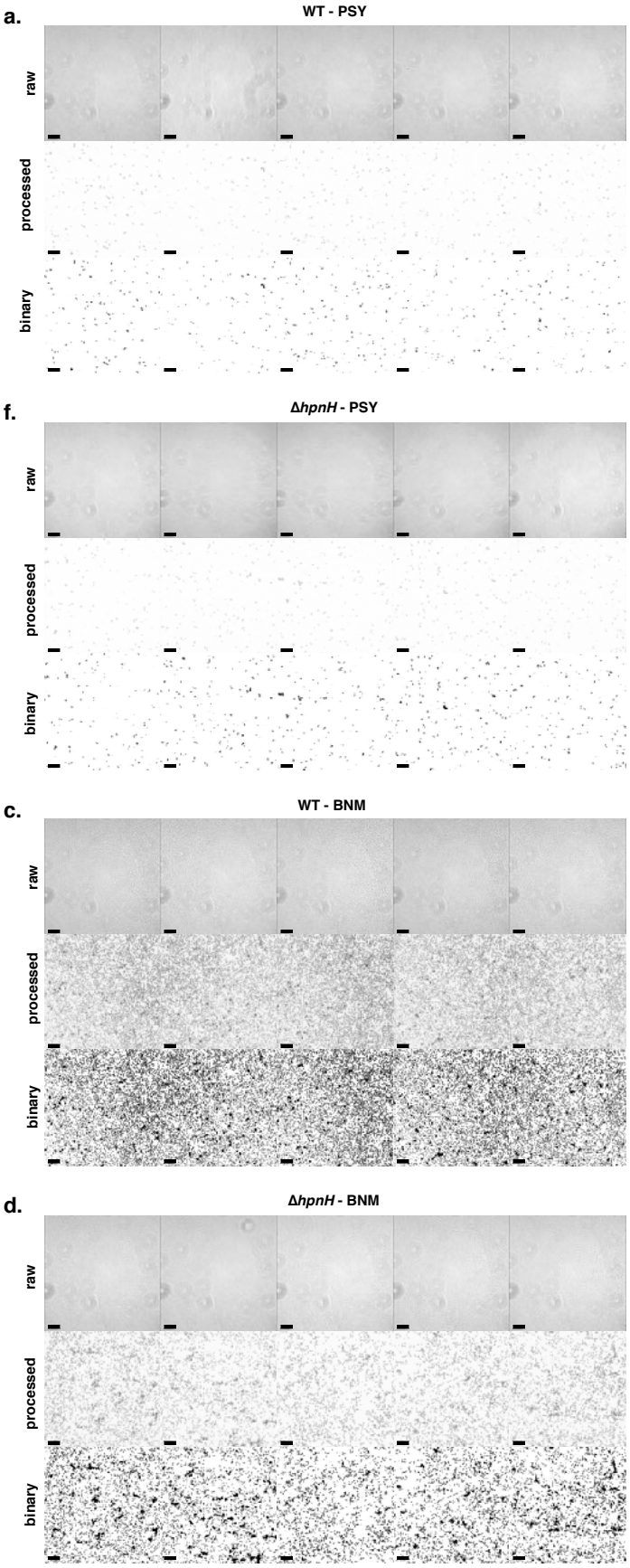

Figure S20. Surface attachment of wild type (**a,c**) and Δ*hpnH* (**b,d**) incubated on glass coverslips in various media. For each panel, raw phase images (top row), background-subtracted images (middle row), and binary images with cells shown in black (bottom row) are shown. Scale bars represent 20 µm.